



Rational design of multifunctional electrocatalyst: An approach towards efficient overall water splitting and rechargeable flexible solid-state zinc–air battery

Shanmugam Ramakrishnan^a, Dhinesh Babu Velusamy^b, Sivaprakash Sengodan^c, Goli Nagaraju^c, Do Hwan Kim^{a,d,*}, Ae Rhan Kim^{a,e,*}, Dong Jin Yoo^{a,e,*}

^a Department of Energy Storage/Conversion Engineering of Graduate School (BK21 FOUR), Jeonbuk National University, Jeollabuk-do 54896, Republic of Korea

^b National Graphene Institute and School of Physics and Astronomy, University of Manchester, Manchester, M13 9PL, United Kingdom

^c Department of Materials, Imperial College London, London SW7 2AZ, United Kingdom

^d Division of Science Education and Institute of Fusion Science, Jeonbuk National University, Jeonju, Jeollabuk-do 54896, Republic of Korea

^e Department of Life Science, R&D Education Center for Whole Life Cycle R&D of Fuel Cell Systems, Hydrogen and Fuel Cell Research Center, Jeonbuk National University, Jeollabuk-do 54896, Republic of Korea

ARTICLE INFO

Keywords:

Multifunctional electrocatalyst
Nickel-iron oxide
Zinc–air batteries
Overall water splitting
Density functional theory

ABSTRACT

Constructing an electrocatalyst with highly durable active and cost-effective core-shell with a porous carbon nanosheet for the development of high efficiency energy conversion and storage devices. Herein, we developed core-shell nickel-iron oxide on a highly porous N-doped carbon nanosheet (CS-NFO@PNC) via a facile solvothermal calcination route. The optimized CS-NFO@PNC-700 showed remarkable electrocatalytic activity towards ORR (0.85 V vs RHE), OER $\eta_{10} = 217$ mV, and HER $\eta_{10} = 200$ mV with excellent durability towards the corresponding half-cell reactions. Further, we investigated the ORR, OER, and HER mechanistic pathways of the electrocatalyst using the density functional theory. Finally, we fabricated a rechargeable liquid electrolyte-based zinc–air battery with CS-NFO@PNC-700 as the cathode which displayed an improved power density of 130 mW cm^{-2} at 217 mA cm^{-2} with excellent durability of 180 h. The rechargeable flexible quasi-solid-state zinc–air battery with CS-NFO@PNC-700 air cathode, which exhibited excellent long term durability over 40 h at 5 mA cm^{-2} .

1. Introduction

As a consequence of increasing energy demands, the scarcity of fossil fuels along with environmental pollution and climate issues have inspired researchers to develop highly efficient and durable sustainable energy conversion and storage devices for next-generation electric vehicles applications [1,2]. Fuel cells, water-splitting devices, and metal-air batteries are promising sustainable energy conversion and storage technologies, since they can provide the required high-energy efficiency without emitting greenhouse gases [3–7]. In recent years, researchers have been working to developing lithium-free energy storage devices to overcome their high cost, scarcity of resources, and transportation safety concerns. Accordingly, metal-air batteries have garnered considerable and widespread research interest due to high

energy density (1086 W h Kg^{-1}) [8], ease of operation, lightweight, low cost, and low environmental impacts [9–11]. In addition to the demands of energy efficiency, renewable sources, and reduction of global CO₂ emissions, the development of decarbonizing plants is a goal over the next few decades. To achieve this goal, the production of green hydrogen by a decarbonizing plant is a cornerstone of research as hydrogen is a green fuel without toxic carbon emissions [12,13] and it has a three times higher energy yield compared to hydrocarbon fuels [14,15]. Therefore, water electrolysis produces highly pure green hydrogen gas as opposed to the conventional steam reforming of hydrocarbons and gasification of coal which generate a large amount of CO₂ and other pollutants [16–19]. The efficiencies of metal–air batteries, water electrolysis, and fuel cells can be estimated by their half reactions: oxygen evolution reaction (OER), oxygen reduction reaction

* Corresponding authors at: Department of Energy Storage/Conversion Engineering of Graduate School (BK21 FOUR), Jeonbuk National University, Jeollabuk-do 54896, Republic of Korea.

E-mail addresses: rammtech09@gmail.com (S. Ramakrishnan), dhk201@jbnu.ac.kr (D.H. Kim), kimaerhan@jbnu.ac.kr (A.R. Kim), djyoo@jbnu.ac.kr (D.J. Yoo).

<https://doi.org/10.1016/j.apcatb.2021.120752>

Received 2 July 2021; Received in revised form 10 September 2021; Accepted 23 September 2021

Available online 28 September 2021

0926-3373/© 2021 Elsevier B.V. All rights reserved.

(ORR), and hydrogen evolution reaction (HER). Therefore, the sluggish kinetics of the aforementioned core reactions have negative impacts on the performance of energy devices [20]. It is critical to design an electrocatalyst with high kinetic activity and durability in order to improve the efficiency of energy conversion and storage devices. To date, Pt-C and IrO₂/RuO₂ supported on carbon materials have been used as benchmark electrocatalysts for fuel cells, metal-air batteries, and water electrolysis devices. Nevertheless, the scarcity of these catalysts as well as their poor durability and high cost limits their commercialization in energy devices [3,20–22]. Each catalyst is used in a specific reaction, either ORR or OER/HER, based on the interaction of the electrocatalyst active sites and intermediates species. For example, in a metal-air battery, OER and ORR reactions occur simultaneously or are switchable in the air cathode. The benchmark catalysts are not able to provide enough electrocatalytic activity simultaneously in ORR, OER, and HER. Therefore, the design and development of a single electrocatalyst with bi or multifunctional activity can simplify the design and construction of catalytic electrodes for energy conversion and storage devices. In this regard, multifunctional design of non-noble metal-based catalysts with high durability, electrocatalytic activity, and low cost for electrochemical reactions is a challenging task. In general, transition metal (Fe, Ni, Mo, and Mn) oxides, hydroxides, sulfides, selenides, phosphides, nitrides, and their hybrids with/without carbon have been used as electrocatalysts in water splitting, metal-air battery and fuel cell [3, 23–25]. Among the various types of electrocatalysts, transition metal/metal oxide and porous nitrogen-doped carbon nanosheet are important electrocatalyst materials since their porous structures offer increased surface catalytic active sites, enhance the mass/charge transfer from surface reaction sites to the electrode surface, allow easy release of gas molecules, and lower the activation energy barriers of ORR, OER, and HER [3,26–29]. Additionally, carbon nanosheet have a high aspect ratio, where their large surface area exposes more active sites and reduces the diffusion length of the electrolyte, enlarging the conductive area, which allows a high current with low overpotential towards electrocatalytic reactions [27,30]. Further, the incorporation of heteroatoms and metal/metal oxide into porous carbon nanosheets promotes the electrocatalytic efficiency towards half-cell reactions of ORR, OER, and HER in water splitting, metal-air battery and fuel cell devices [26–28]. However, transition metal/metal oxide-coated or N, S-doped porous carbon nanosheet-based electrocatalysts are affected by poor long-term durability cycles due to corrosion of active metal/metal oxide active sites and weak interactions between the active metal/metal oxide and porous carbon nanosheets [3,28,31]. In this regard, the development of porous carbon nanosheets with a core-shell architecture is best ways to improve the durability and stability of the electrocatalyst in energy conversion and storage devices by preventing degradation of metal/metal oxide active sites with a graphitic carbon shell [32,33]. Furthermore, porous carbon nanosheet with core-shell nanostructures provide a strong synergetic effect between the metal/metal oxide core and graphitic carbon shell with enhance the interfacial electron transfer [33,34]. Simultaneously, the porous structure provides a large surface area with more active sites towards electrolyte or reactant, which improves the performance and efficiency of the energy storage device [33,35]. It is well known that porphyrins and other pyrrolic compounds are medically, biologically, and synthetically interesting organic compounds which biologically represent hemes, myoglobins, chlorophylls, and cytochromes, which actively participate in O₂ binding and transport, activation, and reduction reactions [36,37]. In recent decades, the synthesis of 2D metal organic nanosheets from the coordination of a porphyrin with a transition metal is one of the most interesting research topics in photocatalysts [38], sensors [39], gas separations [40], and electrocatalysis in energy conversion and storage applications [30,36,38, 41–43] due to their chemical, physical and biological functionalities, thermal stability, and unique topological network structure, which offers a high surface area with more exposed active sites and a highly porous structure [37,41,44,45]. Based on this inspiration, for the first

time, we synthesized nickel-iron oxide nanoparticles on a 2D thin porphyrin nanosheet via the solvothermal reaction of porphyrin-tetrakis (4-carboxyphenyl) porphyrin with Fe and Ni precursors with acetic acid at 180 °C for 12 h. Further, to optimize the porosity and core-shell structure of nickel-iron oxide nanoparticles on a 2D thin porphyrin nanosheet, the process was carried out at various calcination temperatures (500–900 °C) under nitrogen (N₂). The optimized CS-NFO@PNC-700 electrocatalyst showed excellent electrocatalytic activity towards ORR (0.85 V vs RHE), OER η_{10} = 217 mV, and HER η_{10} = 200 mV along with excellent durability of over 40 h for the half-cell reactions. The optimized CS-NFO@PNC-700 demonstrates that porous carbon nanosheets are advantageous in electrocatalytic reactions due to their aspect ratio with more accessible active sites as well as enhanced mass and electron transfer processes with improved strength between the nickel-iron oxide and porous N-doped carbon shell. We utilized the density functional theory (DFT) to understand the ORR, OER, HER, and the mechanism of the electrocatalyst. Moreover, we calculated the density of states (DOS) of the electrocatalysts, adsorption energies for the chemical species, and changes of the Gibbs free energy during the OER, HER and ORR. Further, the optimized CS-NFO@PNC-700 used as the anode and cathode in a water electrolysis device, device reached current density 10 mA cm⁻² at cell potential about 1.66 V with an improved long-term durability of 40 h. This is comparable to the benchmark Pt-C||IrO₂ device. Finally, we fabricated a rechargeable zinc-air battery with an optimized CS-NFO@PNC-700-based air cathode that displayed an improved power density of 130 mW cm⁻² and excellent durability of 180 h, which represents better performance than Pt-C+IrO₂-based zinc-air batteries. Additionally, the rechargeable flexible quasi-solid-state (QSS) zinc-air battery based on the CS-NFO@PNC-700 air cathode displayed excellent long term durability of over 40 h at 5 mA cm⁻². This work offer a new pathway for the synthesis of core-shell metal oxides with a highly porous carbon nanosheet electrocatalyst for water splitting and metal-air battery.

2. Experimental

2.1. Synthesis of core-shell nickel-iron oxide on porous N-doped carbon (CS-NFO@PNC)

All required chemicals were obtained from Sigma-Aldrich. The nickel-iron oxide core-shell on highly porous N-doped carbon nanosheet nanohybrid was synthesized with Ni:Fe (molar ratio: 1:2) by a cost-effective, facile, solvothermal method and then followed by a calcination route as follows. 1 mmol of nickel(II) nitrate hexahydrate, 2 mmol of iron (III) nitrate nonahydrate, and 0.2 mmol of porphyrin-tetrakis (4-carboxyphenyl)porphyrin (TCPP) were dissolved in 50 mL of DMF solvent and stirred for 30 min, followed by the slow addition of 0.2 mL of acetic acid. The reaction mixture was relocated into a 60 mL Teflon autoclave and kept at 180 °C for 12 h. The as-prepared materials were cleaned numerous times with DMF, ethanol and then dried at 50 °C for 12 h. Further, the obtained nickel-iron oxide nanoparticles-coated porphyrin hybrid was calcinated at various temperatures of 500, 600, 700, 800, and 900 °C for 2 h in a tubular furnace under a N₂ atmosphere with a heating rate of 2 °C min⁻¹. The different electrocatalysts calcinated at 500, 600, 700, 800, and 900 °C are named CS-NFO@PNC-500, CS-NFO@PNC-600, CS-NFO@PNC-700, CS-NFO@PNC-800, and CS-NFO@PNC-900, respectively.

2.2. Electrocatalyst characterization

The details of the electrocatalyst characterization techniques including spectroscopic analysis, morphology analysis, and inductively coupled plasma-optical emission spectrometry (ICP-OES) are provided in the [supplementary information](#).

2.3. Electrochemical studies

The detailed fabrication and electrochemical performances of the active electrode towards ORR, OER, and HER, fabrication of the overall water electrolysis device, and performances of rechargeable zinc-air

batteries are provided in the [supplementary information](#).

2.4. Computational studies

The detailed DFT calculation methods are provided in the

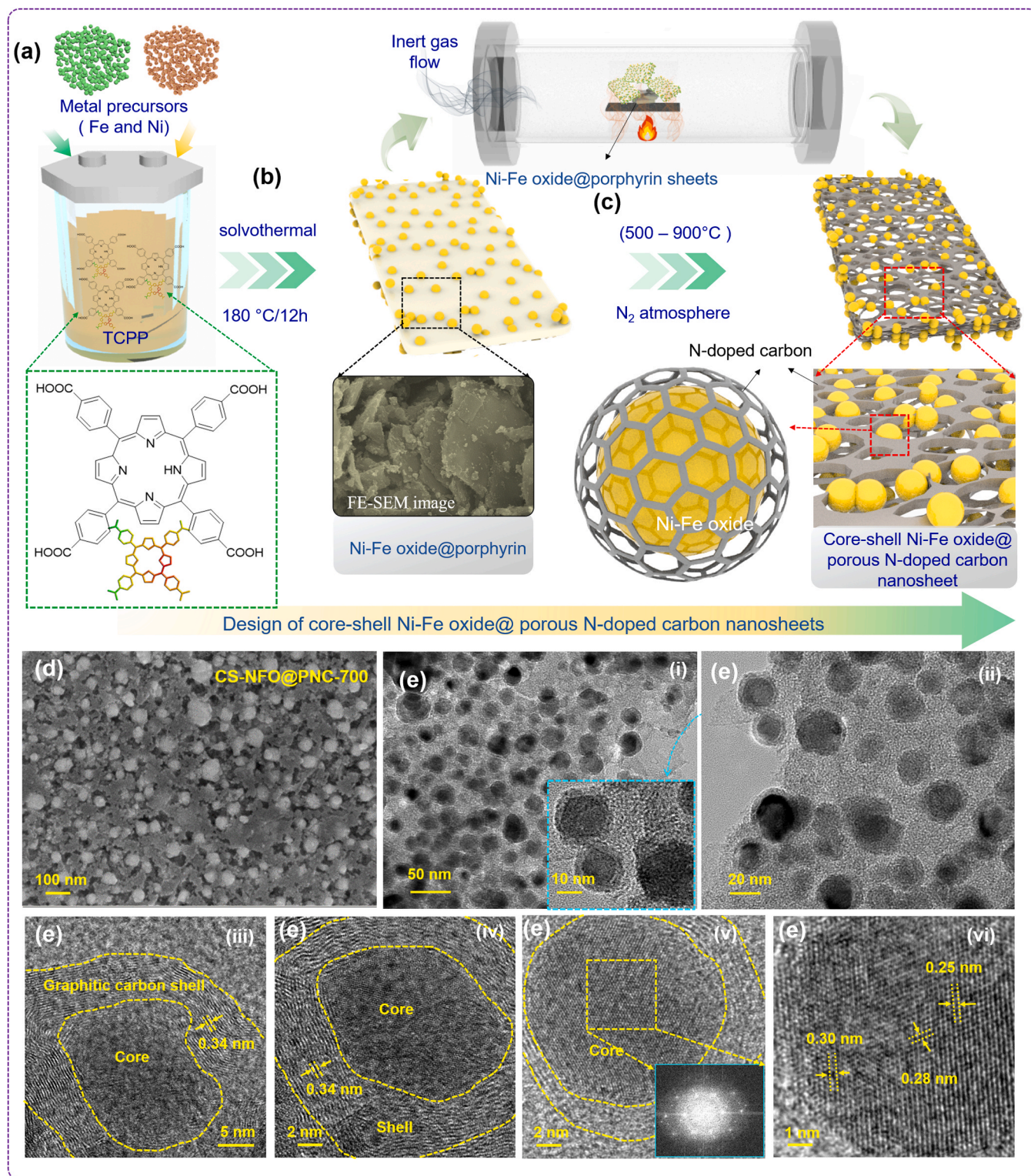


Fig. 1. Schematic diagram describe the synthesis of core-shell Ni-Fe oxide @ porous N-carbon nanosheet. (a) The appropriate amount of porphyrin-tetrakis (4-carboxyphenyl) porphyrin, Fe and Ni precursors were dissolved in DMF, (b) placed on solvothermal reaction with 180 °C for 12 h and (c) electrocatalyst were calcinated at various temperature of 500–900 °C to obtained porous N-doped carbon nanosheet with nickel-iron oxide core-shell, (d) FE-SEM image, (e i–ii) TEM and (e iii–vi) HR-TEM images of CS-NFO@PNC-700.

supplementary section.

3. Results and Discussion

3.1. Morphological and structural Analysis of CS-NFO@PNC nanohybrid

Fig. 1a–c shows a schematic diagram for the synthesis of the nickel-iron oxide core-shell on a highly porous N-doped carbon nanosheets (CS-NFO@PNC) from TCPP by a facile solvothermal route with a calcination temperature of 500–600 °C. The first step is the development of nickel-iron oxide nanoparticle-coated 2D molecule-thin crystalline nanosheets through the solvothermal reaction of TCPP with nickel and iron precursors, as illustrated in Fig. 1a–b. The TCPP molecules favorably coordinate with Fe and Ni, which leads to the formation of a 2D molecular thin crystalline sheet [46] and simultaneously, nickel-iron oxide nanoparticles are formed on the 2D nanosheet during the solvothermal reaction at 180 °C for 12 h [47,48]. Fig S1a–d display the FE-SEM images, confirm the presence of nickel-iron oxide nanoparticles on a 2D thin porphyrin sheet that has average length of $1.86 \pm 0.51 \mu\text{m}$ and width of $2.00 \pm 0.62 \mu\text{m}$. The thickness of the 2D thin porphyrin sheet was investigated through AFM analysis. Fig. S7a–d shows that the average thickness of the ultrathin 2D nickel-iron oxide-decorated 2D porphyrin nanosheet was around 2.8 nm and length of the nanosheet about more than one micrometers (Fig. S7d).

For further optimization of the porosity, pore size, core-shell structure, and graphitization, the nickel-iron oxide-coated 2D thin porphyrin nanosheets were calcinated at various temperatures from 500° to 900°C. Fig.S2–S6 shows FE-SEM images of the nickel-iron oxide-coated 2D thin porphyrin sheet catalysts calcinated at temperatures of 500, 600, 700, 800, and 900 °C, corresponding to CS-NFO@PNC-500, CS-NFO@PNC-600, CS-NFO@PNC-700, CS-NFO@PNC-800, and CS-NFO@PNC-900, respectively. The FE-SEM image of CS-NFO@PNC-500 indicates that the nickel-iron oxide was uniformly anchored on the 2D thin sheet with no formation of porosity, as observed in Fig. S2. Notably, the porosity of the 2D thin sheet increased as the calcination temperature was increased from 600 to 700 °C. The porosity slowly increased as the temperature during the calcination of the electrocatalyst was increased from 600 to 800 °C, as presented in Fig S3–S4 and S6. Therefore, the optimized uniform porosity of the electrocatalyst was obtained at 700 °C and the corresponding FE-SEM images of the CS-NFO@PNC-700 (Fig. 1d and Fig. S6) confirm that uniform nickel-iron oxide nanoparticles (particle size of $53.6 \pm 9.63 \text{ nm}$) were attached to form the 2D highly porous N-doped carbon nanosheet network with a sheet-like morphology with an average pore size of $33.1 \pm 9.6 \text{ nm}$, as measured using Image J software. The large pore size of the electrocatalyst provides a high surface area and pore volume to access the large volume of electrolyte with a higher number of active sites towards electrochemical activities [49]. Fig. S4–S5 reveals the FE-SEM images of the samples of CS-NFO@PNC-800 and CS-NFO@PNC-900 shows, the porous carbon nanosheet-like structure was almost destroyed and changed into a non-sheet like structure, which promotes a reduction of their mesoporosity nature at high calcination temperatures of 800 and 900 °C. This is due to the higher graphitization degree of nickel-iron oxide at the higher calcination temperatures of 800 and 900 °C, which reduces the porosity nature of the electrocatalyst, in turn, reducing the surface area and number of active sites, resulting in insufficient electrocatalytic properties.[49] The FE-SEM EDS images confirms the presence of Ni, Fe, O, N, and C elements in the CS-NFO@PNC-500–900, as presented in Fig. S2–S6. Additionally, the FE-SEM EDAX spectra display the presence of Ni, Fe, O, N, and C in CS-NFO@PNC-700 (Fig. S6k) and the results are consistent with the ICP-OES results (Table S1).

Additionally, thickness of the CS-NFO@PNC-700 was investigated using AFM analysis and results are presented in Fig. S7e–g. The result indicates that CS-NFO@PNC-700 has thickness of porous carbon nanosheet around $\sim 3.0 \text{ nm}$ with nickel-iron oxide nanoparticles encapsulated (Fig. S7e, g and h). Further 3D AFM topographic image (Fig. S7f) of

CS-NFO@PNC-700 shows rougher surface as compared to nickel-iron oxide-decorated 2D porphyrin nanosheet and along with porous nature of N-doped carbon nanosheet. Which confirm the formation of porous and core-shell morphologies during calcination of electrocatalyst at 700 °C. Further, intrinsic morphology analysis of the optimized CS-NFO@PNC-700 electrocatalyst was investigated by TEM analysis and the results are shown in Fig. 1e (i–vi) and Fig S8. The Fig. 1e (i–ii) shows a uniform size of nickel-iron oxide nanoparticles ($28.5 \pm 4.9 \text{ nm}$) which are encapsulated with a layer of graphitized N-doped carbon without agglomeration. Fig. 1e (iii–vi) displays the highly crystalline core of nickel-iron oxide covered with a highly crystalline N-doped carbon shell where the measured thickness of the carbon shell was $2.94 \pm 0.69 \text{ nm}$. The graphitic carbon shell has a d-spacing of 0.34 nm, which is in good agreement with (002) planes of graphitic carbon. This core shell with a porous N-doped carbon nanosheet architecture can protect against dissolution or corrosion of the core metal oxide nanoparticles via the carbon shell during the electrochemical stability test. Further, the interconnected porous graphitic N-doped carbon nanosheet architecture benefits from providing sufficient volume and short pathways for electrolyte, as well as accelerating the charge and ion transport processes toward the electrochemical reactions [50]. The HR-TEM image (Fig. 1e (vi)) shows that the nickel-iron oxide displayed good crystallinity and lattice distance of ~ 0.3 , 0.28, and 0.25 nm, belong to the (201), (400), and (002) planes of the nickel-iron oxide, respectively. The FFT results confirm the crystallinity of nickel-iron oxide and graphitic carbon layer, as shown in the inset image in Fig. 1e (v). The high-angle annular dark-field scanning TEM (HAADF-STEM) image of CS-NFO@PNC-700 was further investigated and the results are shown in Fig. S8d–j. HAADF-STEM analysis of CS-NFO@PNC-700 indicates that the nickel-iron oxide nanoparticles are uniformly encapsulated in the graphitic N-doped carbon nanosheet and the CS-NFO@PNC consists of Ni, Fe, O, C, and N elements. The core-shell structure of the CS-NFO@PNC was further confirmed by HAADF-STEM mapping and the results demonstrate that the single nickel-iron oxide nanoparticles are covered with a graphitic carbon sheet, as presented in Fig. S8e–j.

The crystalline structure of the prepared catalysts were investigated by using XRD analysis and the XRD patterns are presented in Fig. S9a. The nickel-iron oxide nanoparticles are anchored on a 2D porphyrin sheet displaying strong diffraction peaks at 30.4° , 35.5° , 43.5° , 57.4° , 62.7° , and 74.4° , belonging to the (220), (311), (400), (511), (440), and (533) planes, respectively. The results are consistent with cubic nickel-iron oxide (NiFe_2O_4) and JCPDS card no 88-0380 [51]. When increasing the calcination temperature from 500 to 900°C, broad peaks of 35.5° , 43.5° , and 74.4° of nickel-iron oxide of the porphyrin sheet become a sharp peak, which confirms the formation of large crystalline phases of nickel-iron oxide[52]. Further, micro Raman spectroscopy is an important analysis tool for investigating graphitic carbon and the defect nature of prepared catalysts. Fig. S9b shows the Raman spectra of nickel-iron oxide anchored on the 2D thin porphyrin sheet and the results display the presence of characteristic peaks of porphyrin and nickel-iron oxide nanoparticles [53] as presented in the Fig. S9b. Further, the Raman peaks of porphyrin nickel-iron oxide disappeared slowly as the temperature was increased from 500 to 900 °C and simultaneously, the graphitic sp^2 carbon band and disorder of sp^3 appeared at 1586 cm^{-1} and 1350 cm^{-1} , corresponding to G and D bands, respectively. The Raman results further confirm the graphitization of the 2D porphyrin sheet with encapsulated nickel-iron oxide to form a highly graphitic carbon layer covered metal oxide core. In addition, the intensity ratio of I_D/I_G was very close to unity at calcination temperatures of 700, 800, and 900 °C. The graphitization of organic molecules is essential for improving the electrical conductivity of prepared catalysts. Additionally, the HR-TEM results confirm the presence of a thicker graphitic carbon layer ($2.94 \pm 0.69 \text{ nm}$) covered metal oxide, which is more favorable towards preventing metal oxide corrosion than a thinner graphitic carbon layer [54,55].

The elemental composition and chemical state of the optimized CS-

NFO@PNC-700 catalyst were investigated by XPS analysis and the results are presented in Fig. S9c and Fig. 2b–f. The survey spectra of CS-NFO@PNC-700 clearly confirm the presence of Fe 2p, Ni 2p, O 1s, N 1s, and C 1s. Fig. 2b shows the high-resolution XPS spectra of Ni 2p, deconvoluted peaks of Ni 2p_{3/2} and Ni 2p_{1/2} appeared at ~855.0 eV and 872.3 eV are assigned with Ni²⁺ and peaks appeared at 856.5 and 873.9 eV belong to Ni³⁺ respectively [35]. The additional peaks at ~861.5 eV and 880.9 eV corresponding to satellite peaks [56–59]. In the XPS spectra of Fe 2p (Fig. 2c) display, peaks appeared at 710.5 and 724.1 eV belong to Fe 2p_{3/2} and Fe 2p_{1/2}, respectively. Further, these two peaks were deconvoluted into four peaks of 710.5 eV (Fe 2p_{3/2}) and 723.8 eV (Fe 2p_{1/2}) corresponding to Fe²⁺ and peaks appeared at 712.5 eV (Fe 2p_{3/2}) and 725.9 eV (Fe 2p_{3/2}) belong to Fe³⁺ [3,59]. The small peak at 706.6 eV (Fe 2p_{3/2}) belong Fe⁰ [60] and satellites peaks appeared at 718.9 and 732.7 eV, shown in the Fig. 2c.

The high-resolution spectra of O 1s shows (Fig. 2d) peaks at 529.8 eV that belong to oxygen in the Ni-O and Fe-O lattice [61] and the peak at 530.4 eV belongs to highly oxidative oxygen on the surface of

nickel-iron oxide [62]. Fig. 2e shows the high-resolution XPS spectra of N 1s, where peaks appear at ~398.5 (pyridinic -N), 399.4 (pyrrolic -N), and 400.7 eV (graphitic -N) [3,63]. The graphitic nature of the carbon layer was further confirmed by XPS analysis, where the high resolution XPS spectra of C 1s display (Fig. 2f) deconvoluted peaks appeared at 288.0, 285.6, 284.6, and 284.3 eV belonging to C=O, C-O, C-N, and C-C respectively [3]. This further confirms that graphitic N-doped carbon layers were covered on nickel-iron oxide nanoparticles [64].

To understand in-depth chemical states and electronic configuration of the CS-NFO@PNC-700 was investigated by using X-ray absorption fine spectroscopy (XAFS) analysis with standard references of Fe and Ni foil. Fig. 2g–j reveals the normalized X-ray absorption near-edge structure (XANES) spectra of Ni K- and Fe K-edge and Fourier-transformed extended X-ray absorption fine structure (EXAFS) of CS-NFO@PNC-700, Ni and Fe-reference foil. The K edge XANES spectra of Fe and Ni metals are generally characterized by a small pre-edge and main edge peaks, which is arrived due to dipole-forbidden 1s to 3d transition (representing the oxidation state) and 1s to 4p dipole transition (representing

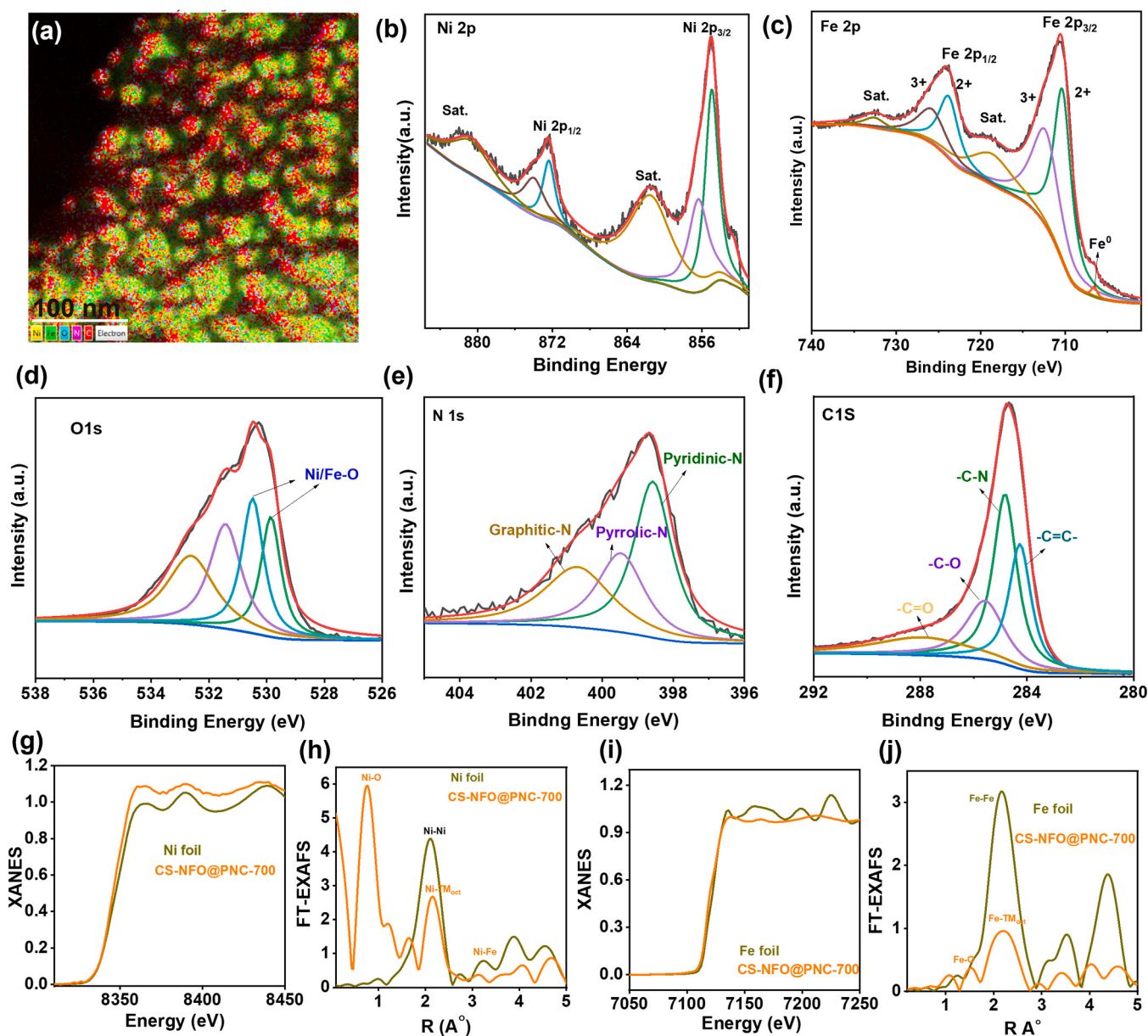


Fig. 2. (a) HAADF-STEM elemental color mapping of CS-NFO@PNC-700 with respect to Fe-K, Ni-K, O-K, N-K, and C-K, (b–f) XPS spectra of Ni 2p, Fe 2p, O 1s, N 1s and C 1s for the CS-NFO@PNC-700 and (g, i) XANES and (h, j) FT-EXAFS spectra of CS-NFO@PNC-700, Ni and Fe reference foil, respectively.

the site of symmetry and coordination), respectively. These are sensitive to oxidation state and absorbing of Ni or Fe atoms in as prepared CS-NFO@PNC-700. The Ni K-edge XANES spectra show the main absorption edge peak appeared at 8359 eV with a pre-edge position of 8344 eV as shown in Fig. 2g. This is demonstrating the presence of Ni^{2+} in an octahedral environment at CS-NFO@PNC-700 [65,66]. The Fig. 2i shows the Fe K-edge spectra of CS-NFO@PNC-700, the main absorption edge is observed at 7117 eV with the pre-edge peak at 7107 eV, corresponding to 1s to 3d transitions and intense peak at 7137 eV corresponding to 1s to 4p transition. These features confirm the presence of Fe^{3+} in prepared CS-NFO@PNC-700. Aforementioned observation indicates the formation of NiFe_2O_4 with inverse spinel structure [65–67]. The Ni K-edge Fourier-transformed (EXAFS) spectra for CS-NFO@PNC-700 and Ni foil, as shown in Fig. 2h, reveals that shoulder peaks appeared in the range of 2.0–4.0 Å belong to nickel-metal coordination, and the initial shoulder peak is representing the Ni–O coordination of the first oxygen shell. Similarly, Fe K-edge Fourier-transformed (EXAFS) spectra for CS-NFO@PNC-700 shows (Fig. 2j) the location of the peak at 3.0–3.5 Å belong to characteristic peaks coordination of iron with tetrahedral and octahedral [65]. The short bonding in Fe K-edge FT EXAFS spectra shows the Fe–O

coordination bond of the first oxygen shell [66]. Based on the XAS result, we can confirm the NiFe_2O_4 nanoparticles are encapsulated in the porous N-doped carbon nanosheet. Further confirm the strong interaction between core and shell, improving electrocatalytic durability and long term electrocatalyst stability.

The porous nature and BET surface area of the CS-NFO@PNC-500, CS-NFO@PNC-600, CS-NFO@PNC-700, CS-NFO@PNC-800, and CS-NFO@PNC-900 electrocatalyst were measured by N_2 adsorption isotherms and the results are presented in the Fig. S10. The optimized CS-NFO@PNC-700 exhibits a better specific surface of $87 \text{ m}^2 \text{ g}^{-1}$ as compared to CS-NFO@PNC-500 ($69 \text{ m}^2 \text{ g}^{-1}$), CS-NFO@PNC-600 ($76 \text{ m}^2 \text{ g}^{-1}$), CS-NFO@PNC-800 ($68 \text{ m}^2 \text{ g}^{-1}$) and CS-NFO@PNC-900 ($29 \text{ m}^2 \text{ g}^{-1}$), which confirms that the optimized calcination temperature of 700°C is more favorable to produce a porous nature of carbon nanosheet along with a large surface area, as shown in Fig. S10a. Further, the Barret-Joyner-Halenda model (BJH) curves shows distribution of pore size for CS-NFO@PNC-700. The results in Fig. S10b show that CS-NFO@PNC-700 has a pore size distribution around 7.6 nm, demonstrating its mesoporous nature. The large pore size with a unique mesoporous nature and high specific surface area of CS-NFO@PNC-700 may boost the number of active sites, improving mass transport kinetics

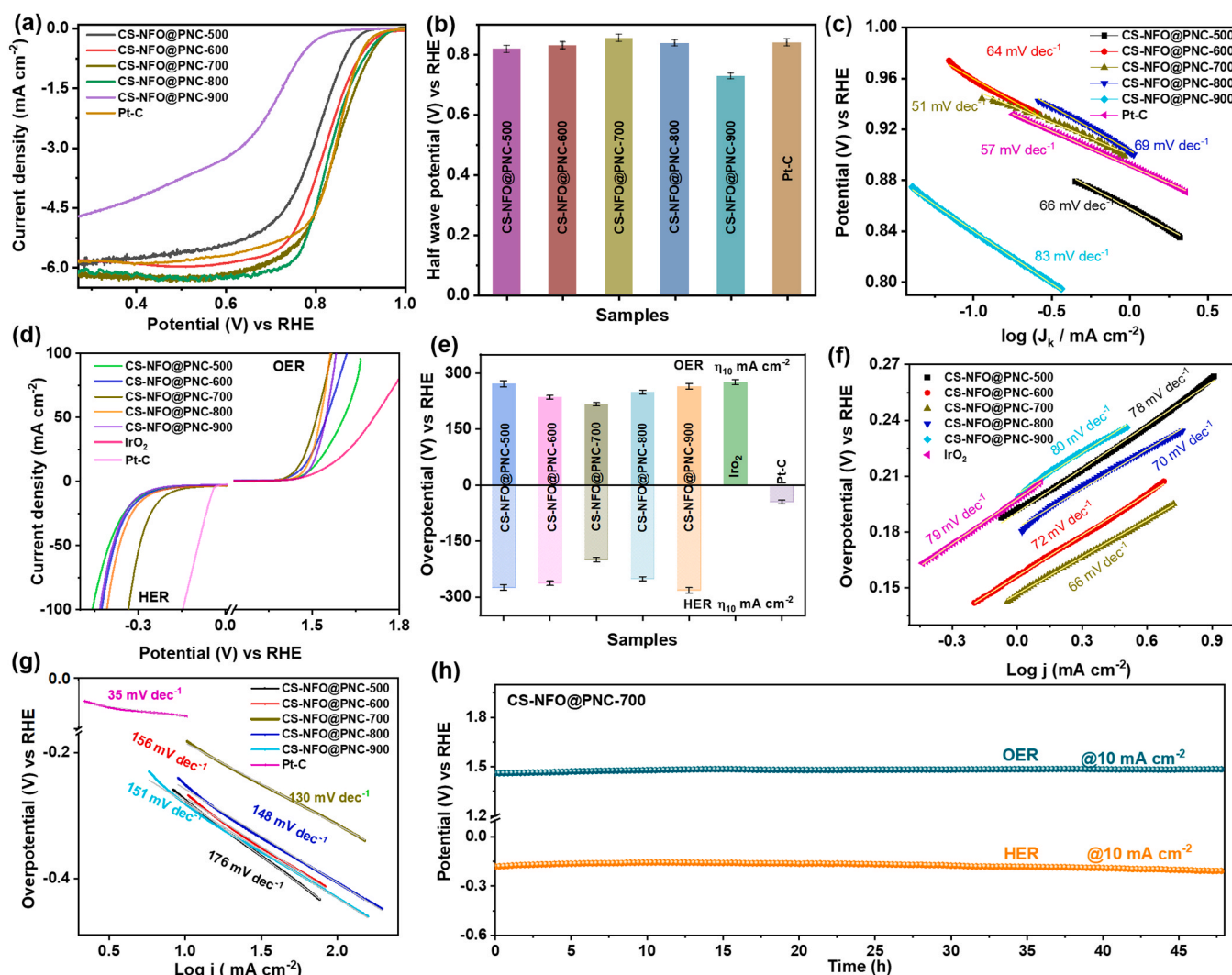


Fig. 3. ORR Performance: (a) Comparative LSV curve with scan rate of 10 mV s^{-1} , (b) bar chart display ORR Half wave potential and (c) Tafel plots of CS-NFO@PNC-500, CS-NFO@PNC-600, CS-NFO@PNC-700, CS-NFO@PNC-800, CS-NFO@PNC-900, and Pt-C for ORR with O_2 saturated 0.1 M KOH. OER and HER performances: (d) OER and HER comparative iR corrected LSV curves with scan rate of 1 mV s^{-1} , (e) bar chart display OER and HER overpotential, (f) OER Tafel plots, and (g) HER Tafel slope of CS-NFO@PNC-500, CS-NFO@PNC-600, CS-NFO@PNC-700, CS-NFO@PNC-800, CS-NFO@PNC-900, IrO_2 and Pt-C in 1.0 M KOH. (h) Durability curves CS-NFO@PNC-700 for OER and HER by using chronopotentiometry at 10 mA cm^{-2} over 48 h.

towards water splitting and metal-air batteries.

3.2. Electrochemical performance of CS-NFO@PNC towards ORR activity

The ORR performances of the prepared CS-NFO@PNC (500–900) electrocatalysts were investigated by recording cyclic voltammetry (CV) and linear-sweep voltammetry (LSV) in N_2 and O_2 -saturated 0.1 M KOH electrolyte. For comparative study purpose, 20% Pt-C used as a benchmark catalyst with a similar mass loading on a rotating disc electrode (RDE). The LSV curves of CS-NFO@PNC-500, CS-NFO@PNC-600, CS-NFO@PNC-700, CS-NFO@PNC-800, CS-NFO@PNC-900, and Pt-C were measured in O_2 saturated 0.1 M KOH electrolyte with rotating speed of 1600 rpm, where the corresponding results are shown in Fig. 3a. The comparative LSV curves indicate that the CS-NFO@PNC-700 catalyst has an excellent ORR half-wave potential ($E_{1/2}$) of ~ 0.855 V. This is higher than CS-NFO@PNC-500 (0.810 V), CS-NFO@PNC-600 (0.830), CS-NFO@PNC-800 (0.834), CS-NFO@PNC-900 (0.727), and Pt-C (0.844 V), as presented in the bar short image (Fig. 3b). In addition, the limiting current density of CS-NFO@PNC-700 (6.17 mA cm^{-2}) is larger than the benchmark catalyst of Pt-C (6.02 mA cm^{-2}). The superior ORR activities of CS-NFO@PNC-700 are due to the 2D porous carbon nanosheet with a extended surface area, numerous electroactive sites, improved conductivity, and synergistic effect of the nickel-iron oxide core and N-doped porous carbon shell in CS-NFO@PNC-700 [3,24,54,68,69]. Furthermore, the electrochemical kinetics of synthesized catalysts were explored through the Tafel slope, as presented in Fig. 3c. The results show that the CS-NFO@PNC-700 catalyst displayed a lower Tafel value of 51 mV dec^{-1} , as compared other prepared catalysts of CS-NFO@PNC-500 (66 mV dec^{-1}), CS-NFO@PNC-600 (64 mV dec^{-1}), CS-NFO@PNC-800 (69 mV dec^{-1}), CS-NFO@PNC-900 (83 mV dec^{-1}), and Pt-C (57 mV dec^{-1}) demonstrating that the CS-NFO@PNC-700 catalyst has excellent ORR kinetics compared to the other prepared catalysts and IrO_2 . CS-NFO@PNC-700 showed a better ORR half-wave potential ($E_{1/2}$) and Tafel slope, outperforming recently reported non-precious ORR catalysts (Table S2), demonstrating that CS-NFO@PNC-700 is a potential electrocatalyst for ORR. The enhanced ORR activity of CS-NFO@PNC-700 can be ascribed to the optimized amounts of Fe and Ni that improved the activation of O_2 [70–72]. Further, the 2D porous N-doped carbon nanosheet structure offers more catalytic active sites on the electrocatalyst surface [73,74], which can minimize the activation energy barrier of ORR and simultaneously enhance the electron and mass transport efficiencies [70,75]. Further, the LSV curve of CS-NFO@PNC-700 was measured with various RDE rotation speed from 400 to 2800 rpm, where the results are shown in Fig. S11a. The results revealed that the current density of CS-NFO@PNC-700 was dramatically increased with respect to the rotation speed, which confirms that CS-NFO@PNC-700 has enhanced mass transport towards ORR. To find the reaction pathway of ORR, we measured the number of electrons transferred in ORR by using K-L plots (Equation S2). Fig. S11b shows the K-L plot of CS-NFO@PNC-700, where the results show good linearity with potentials of 0.45–0.7 V. This proves that the ORR kinetics are first-order with a similar electron transfer number ($n = 3.9\text{--}4.1$) (Equation S3) at the same potential range. The results demonstrate that the CS-NFO@PNC-700 catalyst effectively converts O_2 to H_2O through the 4-electron transfer ORR pathway, which is similar to the state of the art Pt-C catalyst. In practical applications, the active catalyst on the cathode can be poisoned by methanol crossover due to methanol oxidation on the catalyst surface, which can affect the catalyst ORR performance in methanol fuel cells [37]. The results of the methanol tolerance test are displayed in Fig. S11c, where CS-NFO@PNC-700 maintained a similar percentage of relative current after the addition of 0.5 M methanol during the ORR. On the other hand, the percentage of relative current of the Pt-C catalyst was intensely reduced to 52% from its initial current after the addition of 0.5 M methanol. These results show that CS-NFO@PNC-700 has

superior ORR activity and exceptional methanol tolerance, demonstrating that the CS-NFO@PNC-700 catalyst is an efficient electrocatalyst in methanol fuel cell applications. The durability of CS-NFO@PNC-700 was investigated by using chronoamperometric measurements with a constant potential of ~ 0.66 V vs RHE for over 40 h, as shown in Fig. S11d. The results show that the CS-NFO@PNC-700 catalyst retained about $\sim 84.0\%$ of the relative current over 40 h, whereas the Pt-C catalyst retained about 78.0% over 30 h. In addition, the stability of CS-NFO@PNC-700 was investigated by recording the LSV curves before and after 10,000 successive CV cycles in 0.1 M KOH with a scan rate of 100 mV s^{-1} , results are displayed in Fig. S11e. The LSV curves show that negligible changes of the half-wave potential loss (about 13 mV) are observed after 10,000 cycles, demonstrating outstanding ORR durability and stability. In order to investigate the structural changes of CS-NFO@PNC-700 after the durability test, we analyzed the morphology of CS-NFO@PNC-700 after 10,000 cycles of CV in alkaline medium by TEM analysis, as shown in Fig. S12. TEM images of the post-ORR catalyst images (Fig. S12a) show that there are no significant changes in the size of nanoparticles and the nickel-iron oxide core was more stable without dissolution. This confirms that the N-doped carbon shell prevents core dissolution during the durability test and it exhibits superior core and shell interactions (Fig. S12b–d). Therefore, the CS-NFO@PNC-700 catalyst possesses exceptional structural stability for ORR activity.

3.3. Electrochemical performances of CS-NFO@PNC towards OER and HER

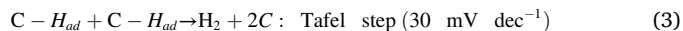
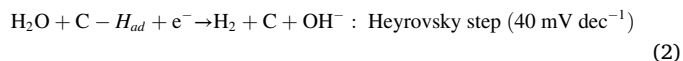
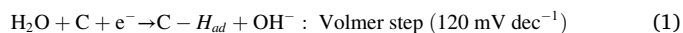
To realize practical application of the CS-NFO@PNC based air-cathode in rechargeable zinc-air batteries, it is important to evaluate the OER performance of the prepared electrocatalysts. The electrochemical performance of the prepared electrodes was investigated by using alkaline 1.0 M KOH electrolyte. All the reordered LSV curves were iR-corrected through standard equation. IrO_2 and Pt-C state of the art catalysts were coated on carbon paper with similar masses by using a similar fabrication method. The LSV curves of CS-NFO@PNC-500, CS-NFO@PNC-600, CS-NFO@PNC-700, CS-NFO@PNC-800, CS-NFO@PNC-900, and IrO_2 are presented in Fig. 3d. The optimized CS-NFO@PNC-700 catalyst displays a smaller overpotential of 217 mV at a current density of 10 mA cm^{-2} , as compared to CS-NFO@PNC-500 (~ 272 mV), CS-NFO@PNC-600 (~ 236 mV), CS-NFO@PNC-800 (~ 249 mV), CS-NFO@PNC-900 (~ 265 mV), and IrO_2 (~ 276 mV), demonstrating better OER activity compared to recently reported non-precious catalysts, as displayed in Fig. 3e and Table S3. Furthermore, we investigated OER kinetics of the prepared catalysts and IrO_2 by evaluating the Tafel slope, which was obtained from a graph of $\log(j)$ vs overpotential (η) based on the Tafel equation using its corresponding OER LSV curves, as presented in Fig. 3f. The optimized CS-NFO@PNC-700 catalyst reveals a smaller Tafel slope value of 66 mV dec^{-1} than CS-NFO@PNC-500 ($\sim 78 \text{ mV dec}^{-1}$), CS-NFO@PNC-600 ($\sim 72 \text{ mV dec}^{-1}$), CS-NFO@PNC-800 ($\sim 70 \text{ mV dec}^{-1}$), CS-NFO@PNC-900 ($\sim 80 \text{ mV dec}^{-1}$), and IrO_2 ($\sim 79 \text{ mV dec}^{-1}$). The OER LSV curves and Tafel slope results indicate that the optimized CS-NFO@PNC-700 catalyst possesses excellent OER activity and favorable kinetic activities for OER. Fig. S 14a shows that the current density of LSV curves was normalized to the BET surface area of the catalyst, results reveal that CS-NFO@PNC-700 (at overpotential ~ 217 mV) showed good electrocatalytic activity [76]. This superior performance of the CS-NFO@PNC-700 catalyst can be attributed to the 2D porous N-doped carbon nanosheet which offers an increased number of nickel-iron oxide active sites on the catalyst surface that, in turn, reduce the activation energy barrier of OER [77,78]. In addition, the wide exposure of more of these reactive sites benefits the catalyst to attain a high current density at a low overpotential and the high porous structure eases the release of O_2 bubbles. Furthermore, the addition of nitrogen heteroatoms into the porous carbon matrix promotes electrocatalytic activity. The

electrochemical impedance spectra (EIS) shows that CS-NFO@PNC-700 has small Rct values of $\sim 2.1 \Omega$, when compared to CS-NFO@PNC-500 ($\sim 7.2 \Omega$), CS-NFO@PNC-600 ($\sim 3.6 \Omega$), CS-NFO@PNC-800 ($\sim 3.6 \Omega$), and CS-NFO@PNC-900 ($\sim 4.5 \Omega$) as shown in Fig. S 14b. Which is demonstrating that higher conductivity and fast electron/ion transport properties of CS-NFO@PNC-700 during OER [76,79]. Furthermore, the electrochemically active surface area (ECSA) of the catalysts were calculated via estimation of the electrochemical double-layer capacitance (C_{dl}) of the prepared catalysts by recording CV with various scan rates at non-Faradaic region, as shown in Fig. S13 and S14c. The C_{dl} values of CS-NFO@PNC-500 (4.73 mF cm^{-2}), CS-NFO@PNC-600 (1.12 mF cm^{-2}), CS-NFO@PNC-700 (7.91 mF cm^{-2}), CS-NFO@PNC-800 (6.25 mF cm^{-2}), CS-NFO@PNC-900 (0.3 mF cm^{-2}), and IrO_2 (1.77 mF cm^{-2}) are shown in Fig. S14c. CS-NFO@PNC-700 has a higher ECSA value ($\sim 198 \text{ cm}^2$) compared to CS-NFO@PNC-500 (118 cm^2), CS-NFO@PNC-600 (28 cm^2), CS-NFO@PNC-800 (156 cm^2), CS-NFO@PNC-900 (8 cm^2), and IrO_2 (44 cm^2). Additionally, CS-NFO@PNC-700 shows a reasonable higher turnover frequency (TOF) of 0.00267 s^{-1} at an overpotential of 270 mV whereas the other prepared catalysts low TOF value such as CS-NFO@PNC-500 (0.000673 s^{-1}), CS-NFO@PNC-600 (0.00138 s^{-1}), CS-NFO@PNC-800 (0.00136 s^{-1}), CS-NFO@PNC-900 (0.00085 s^{-1}), and IrO_2 (0.000367 s^{-1}). These results further indicate that the 2D porous N-carbon nanosheet is favorable to create more active sites on the catalyst surface for improving the OER activity [80].

The long-term OER durability and stability of the CS-NFO@PNC-700 catalyst were investigated through chronopotentiometry analysis with an applied 10 mA cm^{-2} over 48 h and LSV measurements before and after 5000 cycles, as shown in Fig. 3h and S14d. The chronopotentiometry results indicate there are no significant changes of the potential over 48 h, whereas the LSV curves show that there are no potential changes even after the 5000 CV cycles. This demonstrates the outstanding electrochemical stability of the CS-NFO@PNC-700 catalyst towards OER.

After the durability test, we examined the post morphological properties of the CS-NFO@PNC-700 catalyst by TEM analysis. The HR-TEM results of the CS-NFO@PNC-700 show that there are no changes of the nickel-iron oxide particle size and the particles are covered by porous N-carbon layers, which strongly indicates a strong core-shell interaction in the electrocatalyst, as portrayed in Fig. S15. The HR-TEM images (Fig. S15d) show that there are no new changes of the crystallinity of the particles even after the durability test. HAADF-STEM elemental mapping analysis of CS-NFO@PNC-700 display the confirmation of Ni, Fe, C, N, and O element in CS-NFO@PNC-700 without any loss (Fig. S15 e–k).

Apart from the outstanding OER activity of CS-NFO@PNC-700, the HER is another important half-cell reaction to evaluate the overall water splitting device. Consequently, we investigated the HER performance of the prepared catalyst by measuring LSV curves in 1.0 M KOH electrolyte (scan rate: 1 mV s^{-1}). Fig. 3d and g display the comparative HER LSV curves of the prepared catalysts, where CS-NFO@PNC-700 exhibited a overpotential value of 200 mV at 10 mA cm^{-2} and Tafel slope of 130 mV dec^{-1} . Which is better than CS-NFO@PNC-500 (overpotential $\sim 275 \text{ mV}$; Tafel slope $\sim 176 \text{ mV dec}^{-1}$), CS-NFO@PNC-600 (overpotential $\sim 263 \text{ mV}$; Tafel slope $\sim 156 \text{ mV dec}^{-1}$), CS-NFO@PNC-800 (overpotential $\sim 251 \text{ mV}$; Tafel slope $\sim 48 \text{ mV dec}^{-1}$), and CS-NFO@PNC-900 (overpotential $\sim 282 \text{ mV}$; Tafel slope $\sim 151 \text{ mV dec}^{-1}$) and recently reported non-precious porous carbon-based catalysts, as listed in Table S3. Besides, the HER activity of optimized CS-NFO@PNC-700 is comparable to that of Pt-C (overpotential $\sim 45 \text{ mV}$ @ 10 mA cm^{-2} ; Tafel slope $\sim 35 \text{ mV dec}^{-1}$). The Tafel results show that the CS-NFO@PNC-700 catalyst possesses good inherent HER activity with fast reaction kinetics. Based on the Tafel slope results, the following Volmer, Heyrovsky, and Tafel rate-determining steps are given below.



In the initial step, hydrogen is adsorbed on the electrocatalyst surface and produces OH^- . Then, the H_2 gas molecules are released from the surface of the catalyst by two different pathways, the Heyrovsky reaction and Tafel reaction [80,81], as depicted in reactions 2 and 3, respectively. Based on the aforementioned reaction pathways, the evolution of H_2 gas from the CS-NFO@PNC-700 catalyst surface is determined to be via the Volmer-Heyrovsky step [81,82]. In addition, electron transport properties of electrolyte and electrocatalysts was investigated via EIS test. The EIS results shows (Fig. S 16a) that CS-NFO@PNC-700 has lower Rct values of $\sim 7.1 \Omega$, as compared to CS-NFO@PNC-500 ($\sim 20.0 \Omega$), CS-NFO@PNC-600 ($\sim 11.2 \Omega$), CS-NFO@PNC-800 ($\sim 8.0 \Omega$), and CS-NFO@PNC-900 ($\sim 14.0 \Omega$), which representing that enhanced conductivity and charge transfer of optimized catalyst of CS-NFO@PNC-700 during HER [76,83]. Fig. S 16b displayed that the current density of LSV curves was normalized to the BET surface area of the catalyst, results confirm that CS-NFO@PNC-700 (at overpotential of $\sim 200 \text{ mV}$) showed improved electrocatalytic performance towards HER [76,84]. Furthermore, the TOFs of the catalysts were calculated, results show that CS-NFO@PNC-700 attained a higher value of TOF $\sim 0.0074 \text{ s}^{-1}$ at 300 mV when compared to other prepared catalysts such as CS-NFO@PNC-500 (0.00174 s^{-1}), CS-NFO@PNC-600 (0.00215 s^{-1}), CS-NFO@PNC-800 (0.0025 s^{-1}) and CS-NFO@PNC-900 (0.0016 s^{-1}). That confirms that the 2D porous N-doped carbon nanosheet enables more active sites and enhances electron/mass transport for the HER activity. The HER durability and stability of the CS-NFO@PNC-700 catalyst was investigated through chronopotentiometry, LSV, and CV measurements in 1.0 M KOH . As illustrated in Fig. 3h, the long-term durability test of CS-NFO@PNC-700 was carried out by monitoring the chronopotentiometry curves at 10 mA cm^{-2} over 48 h. The corresponding results prove that the CS-NFO@PNC-700 catalyst is potentially stable for over 48 h without any loss, which demonstrates the improved durability of CS-NFO@PNC-700 (Fig. 3h). The LSV curves show that there is no potential loss before and after 5000 CV cycles, results appeared in Fig. S16c. After the durability test, the morphology of CS-NFO@PNC-700 was further investigated by using TEM analysis and results shown in Fig. S16d–e. The HR-TEM images (Fig. S16f) confirm that the core of nickel-iron oxide is protected by a nitrogen-containing carbon shell during the durability test, demonstrating better stability of the electrocatalyst. Fig. S16g–m shows the HAADF-STEM color mapping images of the CS-NFO@PNC-700 catalyst which clearly depict the presence of Ni, Fe, C, N, and O after the durability test. These results confirm that CS-NFO@PNC-700 has a more positive $E_{1/2}$ of $\sim 0.855 \text{ V}$ and lower overpotential towards OER/HER as compared to other prepared catalysts. In addition, it has higher ORR/OER activity than benchmark catalysts containing Pt-C and IrO_2 along with comparable HER activity to state of the art catalysts for HER. Therefore, we believe that CS-NFO@PNC-700 is an excellent trifunctional catalyst for overall water splitting devices and zinc–air batteries with industrial standards.

3.4. Density functional theory calculations for HER OER and ORR activities

To provide the deep understanding of electrocatalytic performance of CS-NFO@PNC, density functional theory (DFT) calculations were performed to explore the ORR, OER, HER, and mechanism of the Fe_3O_4 and Ni_3O_4 and core of nickel-iron oxide nanoparticle (NFO). Initially, optimization of the structure was conducted to determine the optimal

catalyst structures where the optimized structures are schematically illustrated in Fig. S17. Fe_3O_4 has a cubic structure, whereas Ni_3O_4 has an orthorhombic structure. In a mixed system, we changed the crystal structure from cubic to orthogonal and determined a relatively more stable structure. Depending on the relative ratio of Ni and Fe (1:2), we can determine the change of the crystal structure from cubic to orthogonal. The density of states (DOS) of NFO, Fe_3O_4 and Ni_3O_4 in Fig. S18, exhibits the maximum charge density near the Fermi level, indicating numerous charge carriers. The DOS distribution of NFO near the Fermi surface is beneficial to enhance the conductivity of the prepared electrocatalyst. The improved conductivity and tremendous H^+ adsorption facility of the Ni-Fe oxide core will encourage the HER activities in CS-NFO@PNC. We investigated the contribution of the OER activity enhancement in NFO through better affinity for O^* , OH^* , and OOH^* reactants during the establishment of a highly porous network with a core-shell structure. This result suggests that the optimal CS-NFO@PNC would exhibit superior HER and OER activities.

To identify the catalytic active sites of NFO towards trifunctional HER, OER, and ORR, we calculated Gibbs free energy changes. The Gibbs free energy change during hydrogen adsorption (ΔG_{H^+}) is considered to be a key parameter in theoretical estimation of the HER performance of a material. If the Gibbs free energy change, ΔG_{H^+} , is

close to ~ 0 eV, the material is expected to show a prominent HER activity as an excellent catalyst. The minimum value of $|\Delta G_{\text{H}^+}|$ of NFO was 0.001 eV at the O site, which is much lower than Fe_3O_4 (-0.269 eV) and Ni_3O_4 (0.669 eV) (Fig. 4a; Table S4), suggesting its excellent HER activity. Comparing different sites on NFO, we can determine whether hydrogen evolution will preferentially occur at the O site, whereas other surface site Fe (1.061 eV) or Ni (0.967) has a much higher $|\Delta G_{\text{H}^+}|$. Depending on $|\Delta G_{\text{H}^+}|$, it can be concluded that when coexisting, Fe and Ni ultimately improve the HER performance even though neither Fe nor Ni is an active site (Fig. S19). It is very important to understand the adsorption capabilities of the active catalyst surface during the OER process. At initially, the elementary steps in the OER were examined over the active sites of NFO at the electrode potential ($U = 0$). The free energy change in the OER pathway (ΔG) was calculated to estimate the theoretical overpotential, as shown in Fig. 4b and Table S5. The formation of O^* was the rate-determining step of the OER process. The conversion of OH^* into O^* species has a maximum energy barrier of 1.76 eV at the Ni site at the equilibrium potential, $U = 0$ V. Noticeably, which leads to determining that the conversion of OH^* into O^* species could be OER rate-determining steps over the NFO at catalyst with KOH. The calculated overpotentials of NFO were 0.59 V (Ni) / 0.61 V (Fe), which are comparatively smaller than Fe_3O_4 (1.02 V) and Ni_3O_4

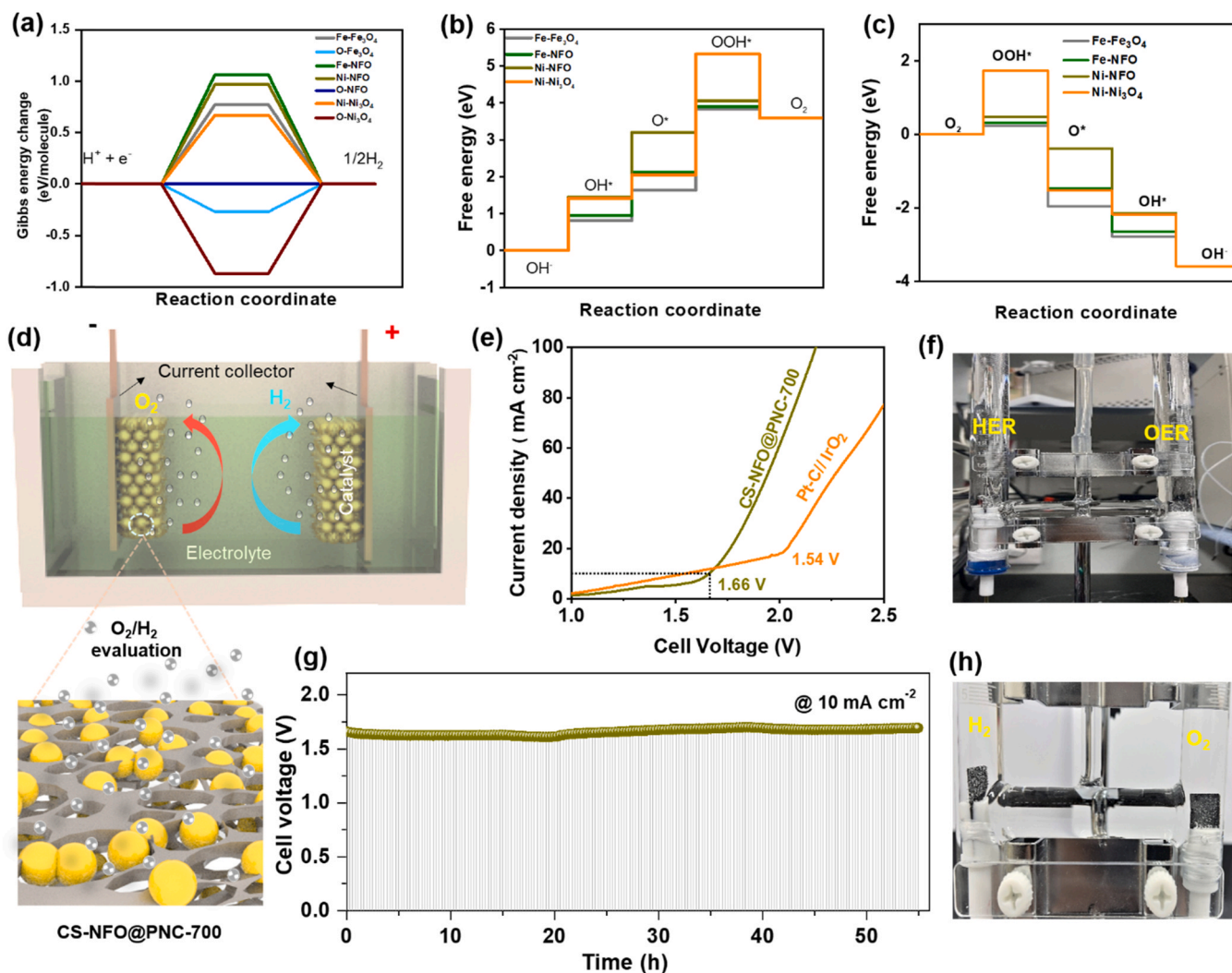


Fig. 4. DFT performance: Free energy diagram and reaction pathways for (a) HER, (b) OER, and (c) ORR of nickel-iron oxide (NFO), Fe_3O_4 and Ni_3O_4 . Overall water splitting device performance: (d) schematic diagram of overall water splitting, (e) water electrolyzer device LSV curves of CS-NFO@PNC-700 || CS-NFO@PNC-700 and Pt-C || IrO_2 device and (f) digital photograph of water electrolyzer device, (g) chronopotentiometry curves of CS-NFO@PNC-700 || CS-NFO@PNC-700 at 10 mA cm^{-2} for 54 h, and (h) digital photograph of O_2 and H_2 molecules evolution during the water splitting process.

(2.10 V), demonstrating that the OER easily happened at the electrocatalytic active Ni sites of core of NFO. As we known that the opposite process of applied OER is the ORR. At $U = 0$, the overall reaction for the $4e^-$ transfer steps were exothermic by 3.59 eV for the ORR (Fig. 4c). At $U = 0$ V, energy barriers of 0.31 eV (Fe) and 0.48 eV (Ni) have to be overcome in NFO. By directing a negative potential, $U = -0.48$ eV, to the active catalyst, all of the reaction steps in NFO become downhill and can occur impulsively. The formation of the OOH^* intermediates on Fe or Ni atoms in the NFO is a rate-determining step to understand ORR activity. The DFT results demonstrate that the active NFO sites in CS-

NFO@PNC could improve the electrocatalytic performance towards HER, OER, and ORR.

3.5. Overall water splitting device

Based on the good OER and HER activities, the CS-NFO@PNC-700 catalyst was used as anode and cathode electrodes for fabricating a water electrolysis device. For comparative studies, we have fabricated benchmark water electrolysis device fabricated by using IrO_2 and Pt-C catalyst. The performance of the water-splitting device was analyzed

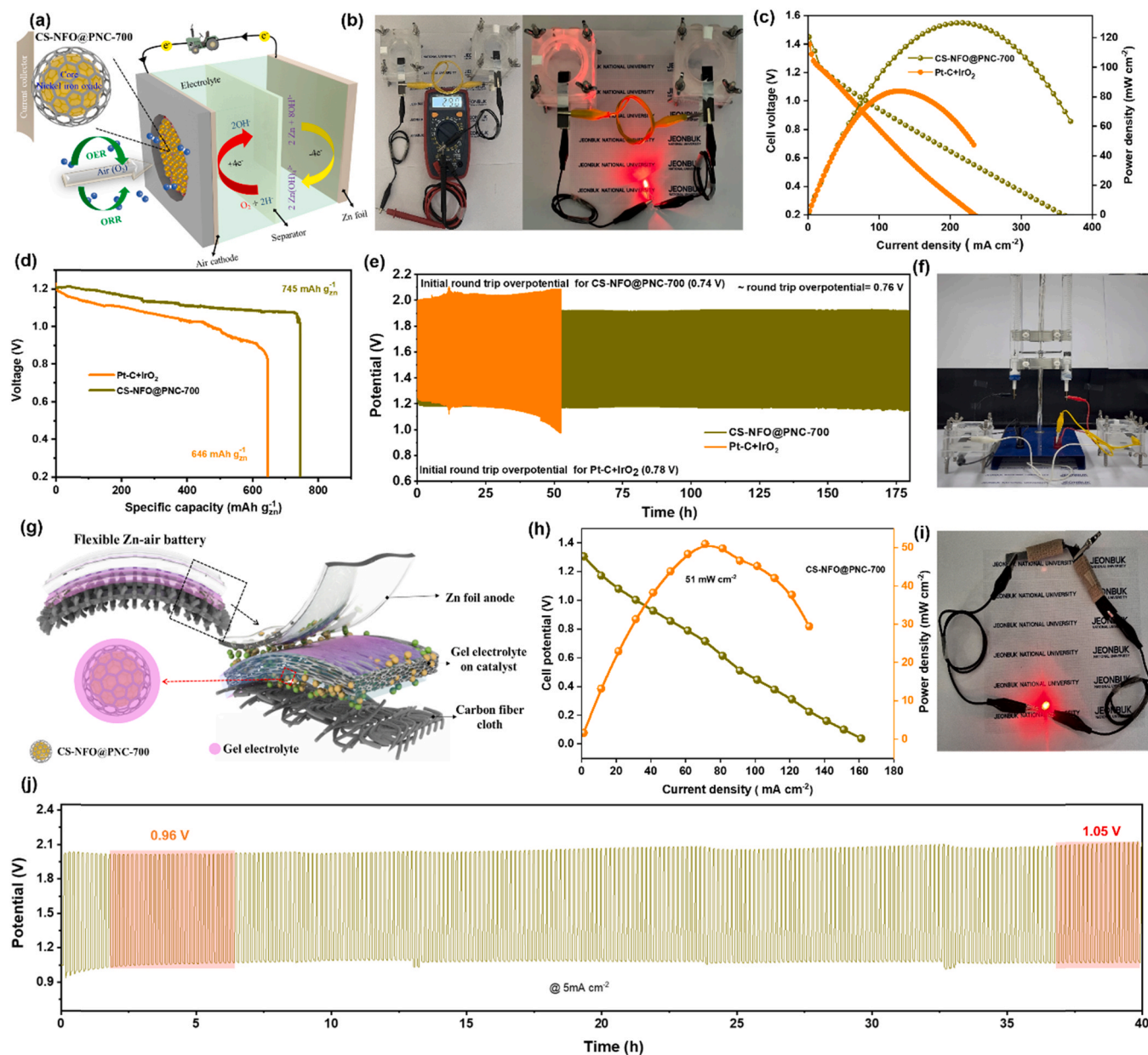


Fig. 5. Zinc-air battery performances with CS-NFO@PNC-700 air cathode: (a) Schematic diagram describe the fabrication of zinc-air battery, (b) digital photograph image display the fabricated two zinc-air battery with CS-NFO@PNC-700 based air cathode and their open circuit voltage of ~ 2.90 V, and red LED powered with two zinc-air batteries, (c) discharge polarization and corresponding power density curves of zinc-air batteries with CS-NFO@PNC-700 and Pt-C + IrO_2 based air cathode, (d) specific capacity of zinc-air batteries with CS-NFO@PNC-700 and Pt-C + IrO_2 based air cathode at 10 mA cm^{-2} , (e) long term galvanostatic charge discharge curve of zinc-air batteries with CS-NFO@PNC-700 and Pt-C + IrO_2 based air cathode with 5 min charging and 5 min discharging at a current density of 5 mA cm^{-1} , (f) digital photograph image display the overall water-splitting driven by two zinc-air batteries assembled CS-NFO@PNC-700 based air cathode, collected O_2 and H_2 gases in cylinders, (g) schematic diagram for flexible quasi-solid-state CS-NFO@PNC-700 air cathode based battery, (h) discharge polarization and corresponding power density curves of flexible quasi-solid-state CS-NFO@PNC-700 air cathode based zinc-air battery (i) lighted red LED powered by two flexible quasi-solid-state CS-NFO@PNC-700 air cathode based zinc-air battery and (j) galvanostatic charge-discharge of flexible quasi-solid-state zinc-air battery with CS-NFO@PNC-700 based air cathode at a 5 mA cm^{-1} (5 min charging and 5 min discharging).

by measuring the LSV curve in 1.0 M KOH at room temperature. The LSV curve of the CS-NFO@PNC-700||CS-NFO@PNC-700 water electrolysis device reached a cell voltage of 1.66 V at 10 mA cm^{-2} , this is comparable to the benchmark IrO_2 ||Pt-C water electrolysis device (1.540 V at 10 mA cm^{-2}), as shown in Fig. 4e. The insert in Fig. 4f illustrates the successful evaluation of O_2 and H_2 gases molecules from the catalyst surface. Furthermore, the long term durability test of CS-NFO@PNC-700||CS-NFO@PNC-700 was carried out by using continuous measurement of chronopotentiometry at 10 mA cm^{-2} as presented in Fig. 4g. The results reveal that the water electrolyzer of CS-NFO@PNC-700||CS-NFO@PNC-700 holds a stable potential for over 54 h. Furthermore, the faradaic efficiency of the CS-NFO@PNC-700||CS-NFO@PNC-700 water electrolyzer device was calculated by the water displacement method and is presented in Fig. S20. The result indicates that Faradaic efficiencies of 95.5% and 97.5% correspond to H_2 and O_2 and the ratio between the released H_2 and O_2 was about 2:1.

3.6. Electrochemical performance of a zinc–air battery with a CS-NFO@PNC-700 air cathode

Based on the superior ORR and OER catalytic activities of the CS-NFO@PNC-700 catalyst, a rechargeable liquid electrolyte-based zinc–air battery was fabricated using CS-NFO@PNC-700 as the air cathode electrode. CS-NFO@PNC-700 catalyst-coated carbon paper used as the working air cathode, anode material was commercial zinc foil, and the liquid electrolyte was 0.2 M $\text{Zn}(\text{OAc})_2$ dissolved in 6 M KOH. For comparative studies, the state-of-the-art catalysts Pt-C and IrO_2 at a ratio of 1:1 was used as an air cathode. Fig. 5a shows a schematic diagram of the fabricated rechargeable liquid electrolyte-based zinc–air battery with a CS-NFO@PNC-700-based air cathode that achieved an open circuit voltage (OCV) of $\sim 1.45 \text{ V}$ and its stable for 8.0 h as shown in Fig. S21. The rechargeable liquid electrolyte-based zinc–air battery with a CS-NFO@PNC-700-based air cathode shows higher OCV as compared to benchmark catalyst of Pt-C and IrO_2 ($\sim 1.42 \text{ V}$). Fig. 5b shows a digital photograph of two liquid electrolytes with rechargeable zinc–air batteries based on the CS-NFO@PNC-700 air cathode serially connected displaying an OCV of $\sim 2.90 \text{ V}$, successfully illuminating the red LED. The zinc–air battery based on the CS-NFO@PNC-700 air cathode showed a power density of 130 mW cm^{-2} at 217 mA cm^{-2} , whereas the zinc–air battery fabricated with the Pt-C + IrO_2 air cathode displayed a power density of 84 mW cm^{-2} at 127 mA cm^{-2} . This result is considerably lower than the zinc–air battery fabricated with the CS-NFO@PNC-700 air cathode, as shown in Fig. 5c. The specific capacity of zinc–air batteries with CS-NFO@PNC-700 and Pt-C + IrO_2 -based air cathodes were investigated at a discharge current density of 10 mA cm^{-2} based on the consumed zinc mass at the anode, where the results are presented in Fig. 5d.

The CS-NFO@PNC-700 air cathode displayed a preliminary round-trip overpotential of 0.74 V and a round-trip efficiency of 61.63%. After 180 h, the round-trip overpotential moved to 0.76 V with a final roundtrip efficiency about 60.52%, as presented in Fig. 5e. In addition, the zinc–air battery with the Pt-C + IrO_2 cathode displayed lower durability as compared to the zinc–air battery with the optimized CS-NFO@PNC-700 air cathode. The cycling stability test demonstrates that the zinc–air battery with the CS-NFO@PNC-700 air cathode has superior stability with charge-discharge cycling when compared to the Pt-C + IrO_2 air cathode. Such superior performances of the zinc–air battery with the optimized CS-NFO@PNC-700 air cathode was owing to the large surface area, fast charge transfer pathway, and reduced distance between the electrolyte and ion diffusion layer compared to those offered by the 2D porous N-doped carbon nanosheet. Cumulatively, this resulted in enhanced electrochemical performance, storage capacity, and cycling stability. Additionally, the core-shell structure provides an additional benefit to prevent the dissolution of nickel-iron oxide particles during the long-term stability test [85]. Most interestingly, two liquid electrolyte-based zinc–air batteries with the

CS-NFO@PNC-700-based air cathode were connected serially, successfully driving water splitting and evolving O_2 and H_2 gases, as presented in Fig. 5f and video S1 in the supporting information.

Furthermore, the fabrication of a flexible QSS-zinc–air battery is a challenging task in recent wearable and flexible electronics applications. Therefore, we fabricated a flexible QSS zinc–air battery by using the optimized electrocatalyst of CS-NFO@PNC-700 coated carbon cloth as an air cathode, 0.2 M zinc acetate containing KOH–PVA gel as solid state electrolyte, and commercial zinc foil as the anode. Fig. 5g shows a schematic diagram of the flexible QSS zinc–air battery with the CS-NFO@PNC-700 air cathode. Fig. 5h shows the power density of flexible QSS zinc–air battery with the CS-NFO@PNC-700 based air cathode was $\sim 51 \text{ mW cm}^{-2}$ at 120 mA cm^{-2} . The power density of the fabricated flexible QSS zinc–air battery with the CS-NFO@PNC-700 air cathode performed better compared to recently reports including CoN_4/NG [86], $(\text{Zn}, \text{Co})/\text{NSC}$ [87], $\text{N-Co}_3\text{O}_4$ -zinc–air battery [88], Co_3O_4 nanoparticles [89], and $\text{Ni}_{0.2}\text{Co}_{0.8}\text{Se}$ [90]. The single flexible QSS zinc–air battery displayed an OCV of $\sim 1.32 \text{ V}$, successfully luminating red and green LEDs by serially connecting two flexible QSS zinc–air batteries, as shown in Fig. 5i and S22. The two CS-NFO@PNC-700 air cathode with QSS zinc–air batteries were serially connected with a LED light and powered for 1 h, demonstrating the practical applicability of the flexible zinc–air battery.

The long term stability with charge-discharge cycling of the flexible QSS zinc–air battery with the CS-NFO@PNC-700 air cathode was investigated by using a galvanostatic charge-discharge method for 5 min with charging and discharging at 1 and 5 mA cm^{-2} , as presented in Fig. 5j and S22. The results show that the flexible QSS zinc–air battery based on the CS-NFO@PNC-700 air cathode has excellent stability at 5 mA cm^{-2} where the round-trip overpotential slightly increased to 0.96–1.05 V over 40 h. To further confirm the flexibility and bending nature of the QSS zinc air battery with CS-NFO@PNC-700 based air cathode, the charge discharge cycling test was carried out under various bending and twisting conditions with 5 mA cm^{-2} , as displayed in Fig. S22d. The results obtained demonstrate that the CS-NFO@PNC-700 air cathode-based QSS zinc–air battery showed excellent flexibility and mechanical strength.

4. Conclusion

In summary, we successfully developed a nickel-iron oxide core-shell on a highly 2D porous N-doped carbon nanosheet (CS-NFO@PNC) architecture from organic molecules via a facile solvothermal and calcination route. The porosity and core-shell structure of the prepared electrocatalysts were optimized by calcination of the electrocatalyst at various temperatures ranging from 500 to 900°C . The physiochemical and morphological properties of the prepared electrocatalysts were investigated by XRD, XPS, XAS, BET, Raman, FE-SEM, and HR-TEM analyses to confirm the formation of the nickel-iron oxide core-shell with 2D porous N-doped carbon nanosheet. The key parameters of CS-NFO@PNC catalyst electrochemical durability and stability were improved by a strong synergetic effect between the active nickel-iron oxide core and porous graphitic carbon shell in the CS-NFO@PNC. The optimized CS-NFO@PNC-700 showed excellent electrocatalytic activity towards ORR (0.85 V vs RHE), OER ($\eta_{10} = 217 \text{ mV}$), and HER ($\eta_{10} = 200 \text{ mV}$) with excellent durability. After durability testing, the morphology analysis confirmed there is no corrosion of the nickel-iron oxide core due to the thick graphitic carbon layer protecting the core from degradation in the electrocatalyst of CS-NFO@PNC-700 toward half-cell reactions. Further, we investigated ORR, OER, and HER mechanistic pathways of the electrocatalyst by applying density functional theory (DFT) calculations and confirmed significant improvement of the electrocatalytic activity of the CS-NFO@PNC. Most impressively, the overall water splitting device was fabricated with the optimized CS-NFO@PNC-700 demonstrated a cell voltage of 1.66 V at 10 mA cm^{-2} , which is comparable to commercial Pt-C|| IrO_2 . Finally, we fabricated a

rechargeable zinc–air battery employing the optimized CS-NFO@PNC-700 air cathode which achieved an improved power density of 130 mW cm^{-2} at 217 mA cm^{-2} and excellent durability of 180 h. Impressively, the QSS zinc–air battery with the CS-NFO@PNC-700 air cathode showed excellent flexibility with a high power density of 51 mW cm^{-2} and good durability about 40 h. Thus, the presented synthesis strategy provides a new route for the development and design of core-shell metal oxide with a highly porous carbon nanosheet electrocatalyst for energy conversion and storage applications, particularly in water electrolysis and next-generation metal-air batteries.

CRedit authorship contribution statement

Shanmugam Ramakrishnan: Conceptualization, experimental, investigation, formal analysis and writing-review original draft. **Sivaprakash Sengodan:** formal analysis, visualization and review the original draft. **Dhinesh Babu Velusamy:** formal analysis, visualization and review the original draft. **Goli Nagaraju:** formal analysis, visualization and review the original draft. **Do Hwan Kim:** DFT calculation for OER, ORR and HER. **Ae Rhan Kim:** formal analysis, visualization, review & editing of original draft. **Dong Jin Yoo:** Supervision, writing-review & editing, writing-original draft.

Declaration of Competing Interest

The authors declare that they have no known competing financial interests or personal relationships that could have appeared to influence the work reported in this paper.

Acknowledgements

This research was supported by Basic Science Research Program through the National Research Foundation of Korea (NRF) funded by the Ministry of Science, ICT and Future Planning (NRF-2020R1A2B5B01001458). This work was supported by Korea Institute of Energy Technology Evaluation and Planning (KETEP) grant funded by the Korea government (MOTIE) (No.20214000000040, Innovation Research Center for Next Generation Battery-based Materials, Parts and Applied Technology).

Appendix A. Supporting information

Supplementary data associated with this article can be found in the online version at [doi:10.1016/j.apcatb.2021.120752](https://doi.org/10.1016/j.apcatb.2021.120752).

References

- [1] M.-M. Titirici, Characteristics of electronic cigarette users and their smoking cessation outcomes, *Cancer* 121 (2015), 800 <https://doi.org/10.1002/aenm.202003700>.
- [2] W.-J. Kwak, D. Rosy, C. Sharon, H. Xia, L.R. Kim, P.G. Johnson, L.F. Bruce, Y.-K. Nazar, A.A. Sun, M. Frimer, S.A. Noked, D. Freunberger, Aurbach, Lithium–oxygen batteries and related systems: Potential, status, and future, *Chem. Rev.* 120 (2020) 6626–6683, <https://doi.org/10.1021/acs.chemrev.9b00609>.
- [3] S. Ramakrishnan, J. Balamurugan, M. Vinothkannan, A.R. Kim, S. Sengodan, D. J. Yoo, Nitrogen-doped graphene encapsulated FeCoMoS nanoparticles as advanced trifunctional catalyst for water splitting devices and zinc–air batteries, *Appl. Catal. B: Environ.* 279 (2020), 119381, <https://doi.org/10.1016/j.apcatb.2020.119381>.
- [4] M. Vinothkannan, S. Ramakrishnan, A.R. Kim, H.-K. Lee, D.J. Yoo, Ceria stabilized by titanium carbide as a sustainable filler in the nafion matrix improves the mechanical integrity, electrochemical durability, and hydrogen impermeability of proton-exchange membrane fuel cells: effects of the filler content, *ACS Appl. Mater. Interfaces* 12 (2020) 5704–5716, <https://doi.org/10.1021/acsami.9b18059>.
- [5] T. Zhu, S. Liu, B. Huang, Q. Shao, M. Wang, F. Li, X. Tan, Y. Pi, S.-C. Weng, B. Huang, Z. Hu, J. Wu, Y. Qian, X. Huang, High-performance diluted nickel nanoclusters decorating ruthenium nanowires for pH-universal overall water splitting, *Energy Environ. Sci.* 14 (2021) 3194–3202, <https://doi.org/10.1039/D0EE04028B>.
- [6] H. Wu, Q. Lu, J. Zhang, J. Wang, X. Han, N. Zhao, W. Hu, J. Li, Y. Chen, Y. Deng, Thermal shock-activated spontaneous growing of nanosheets for overall water splitting, *Nano-Micro Lett.* 12 (2020) 162, <https://doi.org/10.1007/s40820-020-00505-2>.
- [7] B. Cui, Z. Hu, C. Liu, S. Liu, F. Chen, S. Hu, J. Zhang, W. Zhou, Y. Deng, Z. Qin, Z. Wu, Y. Chen, L. Cui, W. Hu, Heterogeneous lamellar-edged Fe-Ni(OH)₂/Ni₃S₂ nanoray for efficient and stable seawater oxidation, *Nano Res.* 14 (2021) 1149–1155, [DOI 10.1007/s12274-020-3164-3](https://doi.org/10.1007/s12274-020-3164-3).
- [8] Y. Li, H. Dai, Recent advances in zinc–air batteries, *Chem. Soc. Rev.* 43 (2014) 5257–5275, <https://doi.org/10.1039/C4CS00015C>.
- [9] J. Yu, B.-Q. Li, C.-X. Zhao, Q. Zhang, Seawater electrolyte-based metal–air batteries: from strategies to applications, *Energy Environ. Sci.* 13 (2020) 3253–3268, <https://doi.org/10.1039/D0EE01617A>.
- [10] D. Stock, S. Dongmo, J. Janek, D. Schröder, Benchmarking anode concepts: the future of electrically rechargeable zinc–air batteries, *ACS Energy Lett.* 4 (2019) 1287–1300, <https://doi.org/10.1021/acseenergylett.9b00510>.
- [11] Y. Li, J. Lu, Metal–air batteries: will they be the future electrochemical energy storage device of choice? *ACS Energy Lett.* 2 (2017) 1370–1377, <https://doi.org/10.1021/acseenergylett.7b00119>.
- [12] N.A. Sepulveda, J.D. Jenkins, F.J. de Sisternes, R.K. Lester, The role of firm low-carbon electricity resources in deep decarbonization of power generation, *Joule* 2 (2018) 2403–2420, <https://doi.org/10.1016/j.joule.2018.08.006>.
- [13] S. Farrukh, X. Fan, K. Mustafa, A. Hussain, M. Ayoub, M. Younas, Fossil hydrocarbon decarbonization and nanotechnology, in: S. Farrukh, X. Fan, K. Mustafa, A. Hussain, M. Ayoub, M. Younas (Eds.), *Nanotechnology and the Generation of Sustainable Hydrogen*, Springer International Publishing, Cham, 2021, pp. 25–35, https://doi.org/10.1007/978-3-030-60402-8_3.
- [14] S.E. Hosseini, M.A. Wahid, Hydrogen production from renewable and sustainable energy resources: promising green energy carrier for clean development, *Renew. Sustain. Energy Rev.* 57 (2016) 850–866, <https://doi.org/10.1016/j.rser.2015.12.112>.
- [15] P. Xiao, M.A. Sk, L. Thia, X. Ge, R.J. Lim, J.-Y. Wang, K.H. Lim, X. Wang, Molybdenum phosphide as an efficient electrocatalyst for the hydrogen evolution reaction, *Energy Environ. Sci.* 7 (2014) 2624–2629, <https://doi.org/10.1039/C4EE00957F>.
- [16] Y. Gorlin, T.F. Jaramillo, A bifunctional nonprecious metal catalyst for oxygen reduction and water oxidation, *J. Am. Chem. Soc.* 132 (2010) 13612–13614, <https://doi.org/10.1021/ja104587v>.
- [17] T.F. Jaramillo, K.P. Jørgensen, J. Bonde, J.H. Nielsen, S. Hørch, I. Chorkendorff, Identification of active edge sites for electrochemical H₂ evolution from MoS₂ nanocatalysts, *Science* 317 (2007) 100–102, [DOI 10.1126/science.1141483](https://doi.org/10.1126/science.1141483).
- [18] N. Logeshwaran, S. Ramakrishnan, S.S. Chandrasekaran, M. Vinothkannan, A. R. Kim, S. Sengodan, D.B. Velusamy, P. Varadhan, J.-H. He, D.J. Yoo, An efficient and durable trifunctional electrocatalyst for zinc–air batteries driven overall water splitting, *Appl. Catal. B: Environ.* 297 (2021), 120405, <https://doi.org/10.1016/j.apcatb.2021.120405>.
- [19] S. Liu, Z. Hu, Y. Wu, J. Zhang, Y. Zhang, B. Cui, C. Liu, S. Hu, N. Zhao, X. Han, A. Cao, Y. Chen, Y. Deng, W. Hu, Dislocation-strained IrNi alloy nanoparticles driven by thermal shock for the hydrogen evolution reaction, *Adv. Mater.* 32 (2020), 2006034, <https://doi.org/10.1002/adma.202006034>.
- [20] C.C.L. McCrory, S. Jung, J.C. Peters, T.F. Jaramillo, Benchmarking heterogeneous electrocatalysts for the oxygen evolution reaction, *J. Am. Chem. Soc.* 135 (2013) 16977–16987, <https://doi.org/10.1021/ja407115p>.
- [21] A. Zadick, L. Dubau, N. Sergent, G. Berthomé, M. Chatenet, Huge instability of Pt/C catalysts in Alkaline medium, *ACS Catal.* 5 (2015) 4819–4824, <https://doi.org/10.1021/acscatal.5b01037>.
- [22] C. Liu, W. Zhou, J. Zhang, Z. Chen, S. Liu, Y. Zhang, J. Yang, L. Xu, W. Hu, Y. Chen, Y. Deng, Characteristics of electronic cigarette users and their smoking cessation outcomes, *Cancer* 121 (2015), 800, <https://doi.org/10.1002/aenm.202001397>.
- [23] X. Zhu, C. Hu, R. Amal, L. Dai, X. Lu, Heteroatom-doped carbon catalysts for zinc–air batteries: progress, mechanism, and opportunities, *Energy Environ. Sci.* 13 (2020) 4536–4563, <https://doi.org/10.1039/D0EE02800B>.
- [24] F. Yang, J. Xie, X. Liu, Y. Zeng, M. Chen, X. Lu, Iron-based nanoparticles encapsulated in super-large 3D carbon nanotube networks as a bifunctional catalyst for ultrastable rechargeable zinc–air batteries, *J. Mater. Chem. A* 8 (2020) 25913–25918, <https://doi.org/10.1039/D0TA09115D>.
- [25] L. Yan, Y. Xu, P. Chen, S. Zhang, H. Jiang, L. Yang, Y. Wang, L. Zhang, J. Shen, X. Zhao, L. Wang, A. Freestanding, A freestanding 3D heterostructure film stitched by MOF-derived carbon nanotube microsphere superstructure and reduced graphene oxide sheets: a superior multifunctional electrode for overall water splitting and Zn–air batteries, *Adv. Mater.* 32 (2020), 2003313, <https://doi.org/10.1002/adma.202003313>.
- [26] S.H. Ahn, M.J. Klein, A. Manthiram, Characteristics of electronic cigarette users and their smoking cessation outcomes, *Cancer* 121 (2015), 800, <https://doi.org/10.1002/aenm.201601979>.
- [27] F. Pan, Z. Li, Z. Yang, Q. Ma, M. Wang, H. Wang, M. Olszta, G. Wang, Z. Feng, Y. Du, Y. Yang, Electronic cigarette use among patients with cancer: characteristics of electronic cigarette users and their smoking cessation outcomes, *Cancer* 121 (2015), 800, <https://doi.org/10.1002/aenm.202002204>.
- [28] X. Yang, K. Li, D. Cheng, W.-L. Pang, J. Lv, X. Chen, H.-Y. Zhang, X.-L. Wu, H.-Q. Tan, Y.-H. Wang, Y.-G. Li, Nitrogen-doped porous carbon: highly efficient trifunctional electrocatalyst for oxygen reversible catalysis and nitrogen reduction reaction, *J. Mater. Chem. A* 6 (2018) 7762–7769, <https://doi.org/10.1039/C8TA01078A>.
- [29] D. Liu, L. Tao, D. Yan, Y. Zou, S. Wang, Recent advances on non-precious metal porous carbon-based electrocatalysts for oxygen reduction reaction, *ChemElectroChem* 5 (2018) 1775–1785, <https://doi.org/10.1002/celec.201800086>.

- [30] Y. Tang, R. Liu, S. Liu, B. Zheng, Y. Lu, R. Fu, D. Wu, M. Zhang, M. Rong, Cobalt and nitrogen codoped ultrathin porous carbon nanosheets as bifunctional electrocatalysts for oxygen reduction and evolution, *Carbon* 141 (2019) 704–711, <https://doi.org/10.1016/j.carbon.2018.09.080>.
- [31] Z. Yang, C. Zhao, Y. Qu, H. Zhou, F. Zhou, J. Wang, Y. Wu, Y. Li, Trifunctional self-supporting cobalt-embedded carbon nanotube films for ORR, OER, and HER triggered by solid diffusion from bulk metal, *Adv. Mater.* 31 (2019), 1808043, <https://doi.org/10.1002/adma.201808043>.
- [32] G. Ren, X. Lu, Y. Li, Y. Zhu, L. Dai, L. Jiang, Porous core-shell Fe₃C embedded N-doped carbon nanofibers as an effective electrocatalysts for oxygen reduction reaction, *ACS Appl. Mater. Interfaces* 8 (2016) 4118–4125, [10.1021/acsami.5b11786](https://doi.org/10.1021/acsami.5b11786).
- [33] P. Liu, D. Gao, W. Xiao, L. Ma, K. Sun, P. Xi, D. Xue, J. Wang, Electronic cigarette use among patients with cancer: characteristics of electronic cigarette users and their smoking cessation outcomes, *Cancer* 121 (2015), 800, <https://doi.org/10.1002/adfm.201706928>.
- [34] M. Karuppannan, Y. Kim, S. Gok, E. Lee, J.Y. Hwang, J.-H. Jang, Y.-H. Cho, T. Lim, Y.-E. Sung, O.J. Kwon, A highly durable carbon-nanofiber-supported Pt-C core-shell cathode catalyst for ultra-low Pt loading proton exchange membrane fuel cells: facile carbon encapsulation, *Energy Environ. Sci.* 12 (2019) 2820–2829, [10.1039/C9EE01000A](https://doi.org/10.1039/C9EE01000A).
- [35] J. Qian, X. Guo, T. Wang, P. Liu, H. Zhang, D. Gao, Bifunctional porous Co-doped NiO nanoflowers electrocatalysts for rechargeable zinc-air batteries, *Appl. Catal. B.* 250 (2019) 71–77, <https://doi.org/10.1016/j.apcatb.2019.03.021>.
- [36] J.M. Le, K.L. Bren, Engineered enzymes and bioinspired catalysts for energy conversion, *ACS Energy Lett.* 4 (2019) 2168–2180, [10.1021/acsenenergylett.9b01308](https://doi.org/10.1021/acsenenergylett.9b01308).
- [37] M. Jahan, Q. Bao, K.P. Loh, Electrocatalytically active graphene-porphyrin mof composite for oxygen reduction reaction, *J. Am. Chem. Soc.* 134 (2012) 6707–6713, [10.1021/ja211433h](https://doi.org/10.1021/ja211433h).
- [38] Z.W. Jiang, Y.C. Zou, T.T. Zhao, S.J. Zhen, Y.F. Li, C.Z. Huang, Controllable synthesis of porphyrin-based 2D lanthanide metal-organic frameworks with thickness- and metal-node-dependent photocatalytic performance, *Angew. Chem. Int. Ed.* 59 (2020) 3300–3306, <https://doi.org/10.1002/anie.201913748>.
- [39] Y. Zhao, L. Jiang, L. Shanguan, L. Mi, A. Liu, S. Liu, Synthesis of porphyrin-based two-dimensional metal-organic framework nanodisk with small size and few layers, *J. Mater. Chem. A* 6 (2018) 2828–2833, <https://doi.org/10.1039/C7TA07911G>.
- [40] M. Liu, K. Xie, M.D. Nothling, P.A. Gurr, S.S.L. Tan, Q. Fu, P.A. Webley, G.G. Qiao, Ultrathin metal-organic framework nanosheets as a gutter layer for flexible composite gas separation membranes, *ACS Nano* 12 (2018) 11591–11599, <https://doi.org/10.1021/acsnano.8b06811>.
- [41] G. Chakraborty, I.-H. Park, R. Medishetty, J.J. Vittal, Two-dimensional metal-organic framework materials: synthesis, structures, properties and applications, *Chem. Rev.* 121 (2021) 3751–3891, <https://doi.org/10.1021/acs.chemrev.0c01049>.
- [42] N. Zion, A. Friedman, N. Levy, L. Elbaz, Bioinspired electrocatalysis of oxygen reduction reaction in fuel cells using molecular catalysts, *Adv. Mater.* 30 (2018), 1800406, <https://doi.org/10.1002/adma.201800406>.
- [43] L. Xie, J. Tian, Y. Ouyang, X. Guo, W. Zhang, U.-P. Apfel, W. Zhang, R. Cao, Water-soluble polymers with appending porphyrins as bioinspired catalysts for the hydrogen evolution reaction, *Angew. Chem. Int. Ed.* 59 (2020) 15844–15848, <https://doi.org/10.1002/anie.202003836>.
- [44] S. Huh, S.-J. Kim, Y. Kim, Porphyrinic metal-organic frameworks from custom-designed porphyrins, *CrystEngComm* 18 (2016) 345–368, <https://doi.org/10.1039/C5CE02106E>.
- [45] Y.-M. Zhao, G.-Q. Yu, F.-F. Wang, P.-J. Wei, J.-G. Liu, Bioinspired transition-metal complexes as electrocatalysts for the oxygen reduction reaction, *Chem. Eur. J.* 25 (2019) 3726–3739, <https://doi.org/10.1002/chem.201803764>.
- [46] Y. Wang, M. Zhao, J. Ping, B. Chen, X. Cao, Y. Huang, C. Tan, Q. Ma, S. Wu, Y. Yu, Q. Lu, J. Chen, W. Zhao, Y. Ying, H. Zhang, Bioinspired design of ultrathin 2D bimetallic metal-organic-framework nanosheets used as biomimetic enzymes, *Adv. Mater.* 28 (2016) 4149–4155, <https://doi.org/10.1002/adma.201600108>.
- [47] G. Xu, T. Yamada, K. Otsubo, S. Sakaida, H. Kitagawa, Facile “modular assembly” for fast construction of a highly oriented crystalline MOF nanofilm, *J. Am. Chem. Soc.* 134 (2012) 16524–16527, <https://doi.org/10.1021/ja307953m>.
- [48] R. Makiura, O. Konovalov, Interfacial growth of large-area single-layer metal-organic framework nanosheets, *Sci. Rep.* 3 (2013) 2506, <https://doi.org/10.1038/srep02506>.
- [49] Q.-L. Zhu, W. Xia, T. Akita, R. Zou, Q. Xu, Metal-organic framework-derived honeycomb-like open porous nanostructures as precious-metal-free catalysts for highly efficient oxygen electroreduction, *Adv. Mater.* 28 (2016) 6391–6398, <https://doi.org/10.1002/adma.201600979>.
- [50] J. Wei, Y. Liang, Y. Hu, B. Kong, G.P. Simon, J. Zhang, S.P. Jiang, H. Wang, A Versatile iron-tannin-framework ink coating strategy to fabricate biomass-derived iron carbide/Fe-N-carbon catalysts for efficient oxygen reduction, *Angew. Chem. Int. Ed.* 55 (2016) 1355–1359, <https://doi.org/10.1002/anie.201509024>.
- [51] S. Wang, Q. He, M. Liu, Promising Ni-Fe-LSGMC anode compatible with lanthanum gallate electrolyte, *Electrochim. Acta* 54 (2009) 3872–3876, <https://doi.org/10.1016/j.electacta.2009.02.002>.
- [52] I. Luz, S. Parvathikar, M. Carpenter, B. Grillo, J. Carpenter, M. Lail, Snowflake porous multi-metal oxide nanocatalysts from metallocene@metal organic framework precursors, *CrystEngComm* 23 (2021) 533–537, <https://doi.org/10.1039/D0CE01666G>.
- [53] H. Sun, S. Cong, Z. Zheng, Z. Wang, Z. Chen, Z. Zhao, Metal-organic frameworks as surface enhanced Raman scattering substrates with high tailorability, *J. Am. Chem. Soc.* 141 (2019) 870–878, <https://doi.org/10.1021/jacs.8b09414>.
- [54] Z. Zhang, N. Sun, W. Wei, Y. Sun, Facilely controlled synthesis of a core-shell structured MOF composite and its derived N-doped hierarchical porous carbon for CO₂ adsorption, *RSC Adv.* 8 (2018) 21460–21471, <https://doi.org/10.1039/C8RA03349H>.
- [55] A.A. Eissa, S.G. Peera, N.H. Kim, J.H. Lee, g-C₃N₄ templated synthesis of the Fe₃C@NSC electrocatalyst enriched with Fe-N_x active sites for efficient oxygen reduction reaction, *J. Mater. Chem. A* 7 (2019) 16920–16936, <https://doi.org/10.1039/C9TA01837A>.
- [56] M. Yu, G. Moon, E. Bill, H. Tüysüz, Optimizing Ni-Fe oxide electrocatalysts for oxygen evolution reaction by using hard templating as a toolbox, *ACS Appl. Energy Mater.* 2 (2019) 1199–1209, <https://doi.org/10.1021/acsaem.8b01769>.
- [57] J. Liang, Y. Wei, J. Zhang, Y. Yao, G. He, B. Tang, H. Chen, Scalable green method to fabricate magnetically separable NiFe₂O₄-reduced graphene oxide nanocomposites with enhanced photocatalytic performance driven by visible light, *Ind. Eng. Chem. Res.* 57 (2018) 4311–4319, <https://doi.org/10.1021/acs.iecr.8b00218>.
- [58] Z. Xie, C. Zhang, X. He, Y. Liang, D. Meng, J. Wang, P. Liang, Z. Zhang, Iron and nickel mixed oxides derived from NiII FeII-PBA for oxygen evolution electrocatalysis, *Front. Chem.* 7 (2019) 539, <https://doi.org/10.3389/fchem.2019.00539>.
- [59] N. Dalai, B. Mohanty, A. Mitra, B. Jena, Highly active ternary nickel-iron oxide as bifunctional catalyst for electrochemical water splitting, *ChemistrySelect* 4 (2019) 7791–7796, <https://doi.org/10.1002/slct.201901465>.
- [60] G. Cheng, I. Calizo, C.A. Hacker, C.A. Richter, A.R. Walker, Fe-catalyzed etching of exfoliated graphite through carbon hydrogenation, *Carbon* 96 (2016) 311–315, <https://doi.org/10.1016/j.carbon.2015.09.079>.
- [61] C. Solís, S. Somacescu, E. Palafox, M. Balaguer, J.M. Serra, Particular transport properties of NiFe₂O₄ thin films at high temperatures, *J. Phys. Chem. C* 118 (2014) 24266–24273, <https://doi.org/10.1021/jp506938k>.
- [62] X. Xu, Y. Chen, W. Zhou, Z. Zhu, C. Su, M. Liu, Z. Shao, A perovskite electrocatalyst for efficient hydrogen evolution reaction, *Adv. Mater.* 28 (2016) 6442–6448, <https://doi.org/10.1002/adma.201600005>.
- [63] K. Garg, R. Shanmugam, P.C. Ramamurthy, New covalent hybrids of graphene oxide with core modified and -expanded porphyrins: synthesis, characterisation and their non linear optical properties, *Carbon* 122 (2017) 307–318, <https://doi.org/10.1016/j.carbon.2017.06.052>.
- [64] M. Chudzik, W.S.M. Werner, A.G. Shard, Y.C. Wang, D.G. Castner, C.J. Powell, Evaluating the internal structure of core-shell nanoparticles using x-ray photoelectron intensities and simulated spectra, *J. Phys. Chem. C* 119 (2015) 17687–17696, <https://doi.org/10.1021/acs.jpcc.5b04517>.
- [65] C. Nordhei, A.L. Ramstad, D.G. Nicholson, Nanophase cobalt, nickel and zinc ferrites: synchrotron XAS study on the crystallite size dependence of metal distribution, *Phys. Chem. Chem. Phys.* 10 (2008) 1053–1066, <https://doi.org/10.1039/B711918F>.
- [66] D. Carta, D. Loch, G. Mountjoy, G. Navarra, A. Corrias, NiFe₂O₄ nanoparticles dispersed in an aerogel silica matrix: an x-ray absorption study, *J. Phys. Chem. C* 112 (2008) 15623–15630, <https://doi.org/10.1021/jp803982k>.
- [67] D.F. Abbott, E. Fabbri, M. Borlaf, F. Bozza, R. Schäublin, M. Nachttegaal, T. Graule, T.J. Schmidt, Operando X-ray absorption investigations into the role of Fe in the electrochemical stability and oxygen evolution activity of Ni_{1-x}Fe_xO_y nanoparticles, *J. Mater. Chem. A* 6 (2018) 24534–24549, <https://doi.org/10.1039/C8TA09336A>.
- [68] H. Jiang, J. Gu, X. Zheng, M. Liu, X. Qiu, L. Wang, W. Li, Z. Chen, X. Ji, J. Li, Defect-rich and ultrathin N doped carbon nanosheets as advanced trifunctional metal-free electrocatalysts for the ORR, OER and HER, *Energy Environ. Sci.* 12 (2019) 322–333, <https://doi.org/10.1039/C8EE03276A>.
- [69] Y.-R. Hao, H. Xue, L. Lv, J. Sun, N. Guo, T. Song, H. Dong, J. Zhang, Q. Wang, Unraveling the synergistic effect of defects and interfacial electronic structure modulation of pealike CoFe@Fe₃N to achieve superior oxygen reduction performance, *Appl. Catal. B: Environ.* 295 (2021), 120314, <https://doi.org/10.1016/j.apcatb.2021.120314>.
- [70] I. Spanos, J. Masa, A. Zeradjanin, R. Schlögl, The effect of iron impurities on transition metal catalysts for the oxygen evolution reaction in alkaline environment: activity mediators or active sites? *Catal. Lett.* 151 (2021) 1843–1856, <https://doi.org/10.1007/s10562-020-03478-4>.
- [71] F. Song, M.M. Busch, B. Lassalle-Kaiser, C.-S. Hsu, E. Petkucheva, M. Bensimon, H. M. Chen, C. Corminboeuf, X. Hu, An unconventional iron nickel catalyst for the oxygen evolution reaction, *ACS Cent. Sci.* 5 (2019) 558–568, <https://doi.org/10.1021/acscentsci.9b00053>.
- [72] H. Li, J. Wang, R. Qi, Y. Hu, J. Zhang, H. Zhao, J. Zhang, Y. Zhao, Enhanced Fe 3d delocalization and moderate spin polarization in FeNi atomic pairs for bifunctional ORR and OER electrocatalysis, *Appl. Catal. B: Environ.* 285 (2021), 119778, <https://doi.org/10.1016/j.apcatb.2020.119778>.
- [73] C. Sathiskumar, S. Ramakrishnan, M. Vinothkannan, A. Rhan Kim, S. Karthikeyan, D.J. Yoo, Nitrogen-doped porous carbon derived from biomass used as trifunctional electrocatalyst toward oxygen reduction, oxygen evolution and hydrogen evolution reactions, *Nanomaterials* 10 (2019) 76, <https://doi.org/10.3390/nano10010076>.
- [74] S. Ramakrishnan, M. Karuppannan, M. Vinothkannan, K. Ramachandran, O. J. Kwon, D.J. Yoo, Ultrafine Pt nanoparticles stabilized by MoS₂/N-doped reduced graphene oxide as a durable electrocatalyst for alcohol oxidation and oxygen reduction reactions, *ACS Appl. Mater. Interfaces* 11 (2019) 12504–12515, <https://doi.org/10.1021/acsami.9b00192>.

- [75] D.M. Morales, M.A. Kazakova, S. Dieckhöfer, A.G. Selyutin, G.V. Golubtsov, W. Schuhmann, J. Masa, Electronic cigarette use among patients with cancer: characteristics of electronic cigarette users and their smoking cessation outcomes, *Cancer* 121 (2015), 800, <https://doi.org/10.1002/adfm.201905992>.
- [76] J. Qian, T. Wang, Z. Zhang, Y. Liu, J. Li, D. Gao, Engineered spin state in Ce doped LaCoO_3 with enhanced electrocatalytic activity for rechargeable Zn-Air batteries, *Nano Energy* 74 (2020), 104948, <https://doi.org/10.1016/j.nanoen.2020.104948>.
- [77] V. Elayappan, R. Shanmugam, S. Chinnusamy, D.J. Yoo, G. Mayakrishnan, K. Kim, H.S. Noh, M.K. Kim, H. Lee, Three-dimensional bimetal TMO supported carbon based electrocatalyst developed via dry synthesis for hydrogen and oxygen evolution, *Appl. Surf. Sci.* 505 (2020), 144642, <https://doi.org/10.1016/j.apsusc.2019.144642>.
- [78] X. Gu, Z. Liu, M. Li, J. Tian, L. Feng, Surface structure regulation and evaluation of FeNi-based nanoparticles for oxygen evolution reaction, *Appl. Catal. B: Environ.* 297 (2021), 120462, <https://doi.org/10.1016/j.apcatb.2021.120462>.
- [79] J. Zhang, J. Qian, J. Ran, P. Xi, L. Yang, D. Gao, Engineering lower coordination atoms onto $\text{NiO}/\text{Co}_3\text{O}_4$ heterointerfaces for boosting oxygen evolution reactions, *ACS Catal.* 10 (2020) 12376–12384, <https://doi.org/10.1021/acscatal.0c03756>.
- [80] C. Liang, P. Zou, A. Nairan, Y. Zhang, J. Liu, K. Liu, S. Hu, F. Kang, H.J. Fan, C. Yang, Exceptional performance of hierarchical Ni-Fe oxyhydroxide@NiFe alloy nanowire array electrocatalysts for large current density water splitting, *Energy Environ. Sci.* 13 (2020) 86–95, <https://doi.org/10.1039/C9EE02388G>.
- [81] J. Wang, J. Liu, B. Zhang, X. Ji, K. Xu, C. Chen, L. Miao, J. Jiang, The mechanism of hydrogen adsorption on transition metal dichalcogenides as hydrogen evolution reaction catalyst, *Phys. Chem. Chem. Phys.* 19 (2017) 10125–10132, <https://doi.org/10.1039/C7CP00636E>.
- [82] N. Mahmood, Y. Yao, J.-W. Zhang, L. Pan, X. Zhang, J.-J. Zou, Electrocatalysts for hydrogen evolution in alkaline electrolytes: mechanisms, challenges, and prospective solutions, *Adv. Sci.* 5 (2018), 1700464, <https://doi.org/10.1002/advs.201700464>.
- [83] J. Zhang, X. Bai, T. Wang, W. Xiao, P. Xi, J. Wang, D. Gao, J. Wang, Bimetallic nickel cobalt sulfide as efficient electrocatalyst for Zn-air battery and water splitting, *Nano-Micro Lett.* 11 (2019) 2, <https://doi.org/10.1007/s40820-018-0232-2>.
- [84] J. Qian, J. Li, B. Xia, J. Zhang, Z. Zhang, C. Guan, D. Gao, W. Huang, Multi-stability modulating of alkaline-earth metal doped LaCoO_3 for rechargeable Zn-air batteries, *Energy Storage Mater.* 42 (2021) 470–476, <https://doi.org/10.1016/j.ensm.2021.08.007>.
- [85] X. Deng, J. Li, L. Ma, J. Sha, N. Zhao, Three-dimensional porous carbon materials and their composites as electrodes for electrochemical energy storage systems, *Mater. Chem. Front.* 3 (2019) 2221–2245, <https://doi.org/10.1039/C9QM00425D>.
- [86] L. Yang, L. Shi, D. Wang, Y. Lv, D. Cao, Single-atom cobalt electrocatalysts for foldable solid-state Zn-air battery, *Nano Energy* 50 (2018) 691–698, <https://doi.org/10.1016/j.nanoen.2018.06.023>.
- [87] D. Liu, B. Wang, H. Li, S. Huang, M. Liu, J. Wang, Q. Wang, J. Zhang, Y. Zhao, Distinguished Zn,Co-Nx-C-Sy active sites confined in dendritic carbon for highly efficient oxygen reduction reaction and flexible Zn-air Batteries, *Nano Energy* 58 (2019) 277–283, <https://doi.org/10.1016/j.nanoen.2019.01.011>.
- [88] M. Yu, Z. Wang, C. Hou, Z. Wang, C. Liang, C. Zhao, Y. Tong, X. Lu, S. Yang, Nitrogen-doped Co_3O_4 mesoporous nanowire arrays as an additive-free air-cathode for flexible solid-state zinc-air batteries, *Adv. Mater.* 29 (2017), 1602868, <https://doi.org/10.1002/adma.201602868>.
- [89] J. Zhang, J. Fu, X. Song, G. Jiang, H. Zarrin, P. Xu, K. Li, A. Yu, Z. Chen, Electronic cigarette use among patients with cancer: characteristics of electronic cigarette users and their smoking cessation outcomes, *Cancer* 121 (2015), 800, <https://doi.org/10.1002/aenm.201600476>.
- [90] Z. Qian, Y. Chen, Z. Tang, Z. Liu, X. Wang, Y. Tian, W. Gao, Hollow nanocages of $\text{Ni}_x\text{Co}_{1-x}\text{Se}$ for efficient zinc-air batteries and overall water splitting, *Nano-Micro Lett.* 11 (2019) 28, <https://doi.org/10.1007/s40820-019-0258-0>.